An Improved Convection Parameterization with Detailed Aerosol–Cloud Microphysics for a Global Model

ARTI JADAV,[a] DEEPAK WAMAN,[a,b] CHANDRA SHEKHAR PANT,[c] SACHIN PATADE,[a] MARTANDA GAUTAM,[d] VAUGHAN PHILLIPS,[a] AARON BANSEMER,[e] DONIFAN BARAHONA,[f] AND TRUDE STORELMOV[g]

[a] *Department of Physical Geography and Ecosystem Science, Lund University, Lund, Sweden*
[b] *Department of Troposphere, Institute of Meteorology and Climate Research, Karlsruhe Institute of Technology, Karlsruhe, Germany*
[c] *Department of Hydro and Renewable Energy, Indian Institute of Technology Roorkee, Roorkee, India*
[d] *Johannes Gutenberg University, Mainz, Germany*
[e] *Dynamical and Physical Meteorology Section, National Center for Atmospheric Research, Boulder, Colorado*
[f] *Global Modeling and Assimilation Office, NASA Goddard Space Flight Center, Greenbelt, Maryland*
[g] *Department of Geosciences, University of Oslo, Oslo, Norway*

(Manuscript received 27 September 2023, in final form 8 July 2024, accepted 10 July 2024)

ABSTRACT: A new microphysical treatment that includes aerosol–cloud interactions and secondary ice production (SIP) mechanisms is implemented in the convection scheme of the Community Atmosphere Model, version 6 (CAM6). The approach is to embed a 1D Lagrangian parcel model in the bulk convective plume of the existing deep convection parameterization. Aerosol activation, growth processes including collision/coalescence, and three processes of SIP mechanisms, two of which are normally overlooked in atmospheric models, are represented in this embedded parcel model. These microphysical processes are treated with a hybrid bin/bulk scheme and a high spatial and temporal resolution for the integration of the embedded parcel in 1D, allowing vertical velocity to determine the microphysical evolution following the in-cloud motion during ascent. Simulations of an observed case (Midlatitude Continental Convective Clouds Experiment) of a mesoscale convective system in Oklahoma, United States, with a single-column model (SCAM) version of CAM, are compared with aircraft in situ and ground-based observations of microphysical properties from the convection and precipitation. Results from the validation show the new microphysical scheme has a good representation of the ice initiation in the bulk convective plume, including the known and empirically quantified pathways of primary and secondary initiation, with benefits for the accuracy of properties of its supercooled cloud liquid. The sensitivity simulations and use of tagging tracers for the validated simulation confirm that the newly included SIP mechanisms are of paramount importance for convective microphysics and can be successfully treated in the global model.

KEYWORDS: Cloud microphysics; Glaciation; Secondary ice production; Convective parameterization; Cumulus clouds; Single column models

1. Introduction

Aerosol–cloud interactions are crucial for the distribution of precipitation in the present-day climate and for radiative forcings of climate change (Boucher et al. 2013; Forster et al. 2021). Clouds influence Earth's radiation budget by covering about half of the globe on average and contributing the most to the global reflection of shortwave radiation to space (Ramanathan et al. 1989; Boucher et al. 2013; Stubenrauch et al. 2013). Clouds also act similarly to greenhouse gases by absorbing longwave radiation and partially emitting it downward to warm the surface (Raval and Ramanathan 1989). There is an indirect effect on cloud albedo from anthropogenic aerosol emissions, boosting the cloud droplet number concentration and reducing the average droplet size, which makes clouds more reflective (Twomey 1974, 1977; Albrecht 1989). This can offset up to about half of the global warming due to greenhouse gas emissions since preindustrial times (Lohmann 2006). This reduced average droplet size by aerosol emissions also curbs the warm rain process, extending cloud lifetime and further offsetting global warming. Owing to limitations in the microphysical schemes currently used in global models, the corresponding glaciation indirect effect during climate change from ice initiation by aerosol particles is unclear yet potentially significant (Lohmann 2006; Kudzotsa et al. 2016).

Diverse chemical species of aerosol particles in the atmosphere initiate cloud particles by diverse pathways, governing the properties and extent of clouds. The vast majority of the aerosol particles consist of soluble material, and they act as cloud condensation nuclei (CCN) growing by condensation to become cloud droplets in supersaturated conditions such as just above cloud base ("primary or cloud-base droplet activation") (Petters and Kreidenweis 2007; Andreae and Rosenfeld 2008). In deep clouds, especially convective clouds with a vertical acceleration during ascent and precipitation, "in-cloud or secondary droplet activation" occurs either by supersaturation exceeding the peak cloud-base value or by entrainment of the fresh

Denotes content that is immediately available upon publication as open access.

Corresponding author: Arti Jadav, arti.jadav@nateko.lu.se

Publisher's Note: This article was revised on 13 February 2025 to correct a labeling error that occurred in Fig. 9 when originally published.

DOI: 10.1175/JAS-D-23-0175.1

solute aerosols from the environment (Ochs 1978; Pinsky and Khain 2002; Phillips 2022). Fridlind et al. (2004) showed that most of the supercooled cloud droplets in a deep convective storm over Florida were from in-cloud droplet activation of aerosols entrained laterally from the environment into the updraft.

In nature, cloud and aerosol properties vary on spatial scales far smaller than those resolved by climate models. Cloud-scale processes respond to aerosol conditions in various ways, such as changing the cloud albedo (Twomey 1974) and precipitation (Andreae and Rosenfeld 2008). Until parameterizations of clouds and aerosol–cloud interactions at subgrid scales can address these difficulties, model estimates of aerosol–cloud interactions and their radiative effects will have many uncertainties partly because of the nonlinear responses of turbulent in-cloud dynamics to large-scale flows and of cloud properties to the in-cloud ascent statistics. Typically, these nonlinear processes are complex to parameterize. For example, most of the volume of the troposphere is at temperatures below 0°C, where clouds contain ice, so any global model should be able to predict accurately the partitioning of condensed water (liquid and ice) and not just the overall condensed water content.

Ice particles are initiated by primary and secondary ice processes. The primary ice processes include homogeneous freezing and heterogeneous ice nucleation. Heterogeneous ice nucleation occurs on the surface of solid aerosol particles ["ice nucleating particles (INPs)"]. Active INPs have low concentrations in the atmosphere (e.g., a few per liter) (DeMott et al. 2003), and their activity varies substantially with their chemical composition, size, temperature, and supersaturation with respect to ice (Phillips et al. 2008; Kanji et al. 2017). Secondary ice production (SIP) mechanisms work to enhance the ice number and mass concentrations from preexisting ice crystals in precipitating clouds without the action of any aerosols (Yang et al. 2016; Field et al. 2017; Korolev and Leisner 2020). The treatment of all ice initiation processes is essential for predicting the phase of clouds and their radiative properties (Sun and Shine 1994), which then can affect the cloud extent and lifetime (Field and Heymsfield 2015; Mülmenstädt et al. 2015; Gupta et al. 2023).

Numerous observations have shown that in the absence of homogeneous freezing of cloud droplets, the magnitude of the measured ice concentrations in clouds is much higher than those of active INPs in the adjacent environment, providing evidence for the SIP processes in clouds (Cantrell and Heymsfield 2005; Field et al. 2017; Ladino et al. 2017). Some of the proposed SIP mechanisms (Field et al. 2017) are as follows:

- Rime splintering or the Hallett–Mossop process
- Raindrop freezing fragmentation
- Breakup in ice–ice collisions

Sotiropoulou et al. (2021) simulated summer clouds over the West Antarctic Coast and found that including the breakup in ice–ice collisions improved the ice concentrations and suggested this SIP can produce a significant number of ice from a 0.1 L^{-1} of primary ice. Sullivan et al. (2017) showed that including the rime splintering and breakup in ice–ice collisions can enhance the ice number concentration by up to four orders of magnitude in their parcel model simulations. Also, Sotiropoulou et al. (2020) showed that including the rime splintering and breakup in ice–ice collisions gives a better agreement with observation for ice number concentrations. Sullivan et al. (2018) showed that convective precipitation is intensified with the addition of the SIP mechanisms. Laboratory and field studies by Vardiman (1978) and Takahashi et al. (1995) observed fragmentation from ice–ice collisions. Yano and Phillips (2011) did a theoretical study of the impact of this type of SIP on a cloud and demonstrated an explosion in ice number from ice–ice collisions. This SIP is predicted to occur in clouds generally with standard conditions, without any of the restrictions that limit the Hallett–Mossop (HM) process.

Such microphysical complexity of ice initiation is problematic for conventional global models because their parameterizations of deep convection lack realistic treatment of the inherently 3D in-cloud dynamics (Houze 2014).

One such model is the Community Earth System Model (CESM), a fully coupled global model of Earth's climate system (Danabasoglu et al. 2020). The atmospheric component model of CESM is CAM6 and is intended to simulate the thermodynamics, dynamics of the atmosphere, radiative forcing, microphysics and macrophysics of clouds, and aerosol and aerosol chemistry.

CAM6 contains a large-scale cloud scheme (Morrison and Gettelman 2008) and a convective cloud scheme (Zhang and McFarlane 1995; Song and Zhang 2011). The unmodified public version of CESM has a convection scheme by Zhang–Macfarlane (hereafter as ZM) (Zhang and McFarlane 1995) in which the convective cloud microphysics is treated by Song and Zhang (2011) (hereafter as SZ11). The ZM scheme consists of a bulk plume that is intended to be representative of an ensemble of plumes and assumes a fractional entrainment rate whose bulk value is limited by the thermodynamics of the large-scale atmosphere. However, in nature, real plumes vary in depth, width, and ascent within any given mesoscale cloud system with dynamical properties that have a strongly nonlinear impact on the microphysical properties of each plume (Donner et al. 2001). Thus, the mean convective forcing from all plumes of ascent is not equal to the convective forcing of the mean of these plumes in all situations, in view of the nonlinearity. For example, when clouds attain a critical depth, they can suddenly develop precipitation by the warm rain process (Khain et al. 2004).

Additionally, in CAM6, the representation by SZ11 of the interaction between aerosols and cloud ice in deep convection has limited realism in some respects. First, the SZ11 scheme does not represent graupel/hail explicitly, whereas in nature, the richness of supercooled cloud liquid in fast convective ascent promotes riming growth and graupel/hail production. For example, hailstorms are convective clouds. Second, the SZ11 scheme treats primary ice following Liu and Penner (2005) depending on the conditions of aerosol chemistry and loading, in addition to spontaneous freezing of the cloud liquid at the top of the mixed-phase region, namely, "homogeneous freezing of cloud droplets." For heterogeneous ice nucleation, the treatment by Liu and Penner (2005) includes immersion freezing, deposition/condensation nucleation, and contact freezing based on classical heterogeneous ice nucleation theory. Yet, classical nucleation theory tends to overpredict INP activity at

long times unless the full statistical distribution of efficiencies of active sites is treated carefully (Marcolli et al. 2007; Jakobsson et al. 2022).

Third, for homogeneous freezing, all cloud droplets and raindrops reaching levels near about −40°C are correctly assumed homogeneously to freeze to form ice. However, there are issues in predicting the cloud-ice concentration in the anvil cirriform outflow from convective updrafts because the total evaporation of some fraction of the cloud droplets ascending through the layer of homogeneous freezing (about −37° to −36°C) is not included. Heymsfield et al. (2005) and Phillips et al. (2007) underline the impact of this preferential evaporation of the smaller droplets.

Furthermore, there are processes of ice initiation that are known and treated by some recent cloud models (e.g., Huang and Wu 2022) but overlooked by SZ11 in the ZM scheme. Recent measurements and studies indicate the central role of a variety of SIP processes (Mace et al. 2009; Field et al. 2017; Huang et al. 2017; Phillips et al. 2017b; O'Shea et al. 2021; Atlas et al. 2022). The SZ11 scheme uses the HM process of rime splintering by ice precipitation for the representation of SIP (Storelvmo et al. 2008; Gettelman et al. 2010; SZ11).

Last, in the current implementation of SZ11 convective microphysics in CAM6, a limitation arises from the simplistic treatment of in-cloud droplet activation from aerosols. In nature, most droplets well above the level of onset of precipitation are from in-cloud droplet activation in deep convection because most of the primary droplets from cloud base are accreted onto the precipitation, and consequently, the equilibrium supersaturation rises perhaps exceeding the peak at cloud base (Ochs 1978; Pinsky and Khain 2002; Fridlind et al. 2004; Phillips et al. 2007; Phillips 2022). It is the equilibrium supersaturation S_{eq} that drives in-cloud activation (Rogers and Yau 1989) and is calculated as follows:

$$S_{eq} \propto \frac{w_{up}}{\mathrm{CDNC} \times D_{droplet}}, \tag{1}$$

where w_{up} is the vertical velocity, CDNC is the cloud droplet number concentration, and $D_{droplet}$ is the mean diameter of the cloud droplet.

Although the current implementation by SZ11 estimates this equilibrium supersaturation, at in-cloud levels to treat in-cloud activation, this in-cloud droplet activation is treated by approximating the number of aerosols lost by activation with the current droplet concentration. This is not necessarily a realistic approximation because, in natural deep ascent, most cloud droplets are lost by accretion onto precipitation, and so their number concentration is much lower than that of all CCNs lost by activation (Ochs 1978; Phillips 2022).

Regarding the wider ZM scheme in the current version of CAM6, mass flux transfer between clouds and their surroundings is evaluated from prescribed vertical profiles of entrainment and detrainment rates in the grid column. Concerning the dynamics of convective clouds, entrainment and detrainment are difficult to measure in observations or to infer in a detailed cloud model. Their treatment in any convective parameterization is inevitably a major source of error.

Currently, in the ZM scheme of CAM6, detrainment is artificially set to zero below the level of the maximum entrainment rate. Detrainment is assumed to be restricted to levels where the entrainment rate (fractional change in updraft mass flux per unit height) decreases with height (Zhang and McFarlane 1995).

There are two problems with this treatment of detrainment. First, in natural deep convection, detrainment happens when mixed drafts reach their levels of dilute neutral buoyancy (Emanuel 1993; Takahashi and Luo 2012; Takahashi et al. 2017). Depending on the degree of dilution when entraining environmental air mixes with the air from cloud base, the mixed drafts can be positively or negatively buoyant and will move either upward or downward to their level of dilute neutral buoyancy where they may detrain according to Emanuel (1993) and Grandpeix et al. (2004). Hence, consequently, there is no physical reason to restrict detrainment to be only above the level of maximum entrainment. Second, there are numerical challenges to infer the entrainment rate (Zhang and McFarlane 1995, p. 413), and in our offline simulations [section 2d(2)], we find often the maximum entrainment rate is very high in the upper troposphere. For all these reasons, arguably a more realistic treatment of detrainment is from analysis of simulations by the cloud-resolving model (Bechtold et al. 2008; Derbyshire et al. 2011).

The goal of the present paper is to provide a more realistic treatment of the aerosol–cloud interaction in a global model, addressing the limitations mentioned above. Focus is given to resolving, in deep convection, the many processes of initiation of cloud droplets and ice particles in the global model.

The approach in the present study is to embed a Lagrangian parcel model in the existing bulk convective plume of the deep convection parameterization. The ascent of the cloudy parcel is traced from below cloud base to cloud top. Such an approach with a Lagrangian framework offers a valuable way to evaluate the aerosol–cloud interaction and impacts on meteorological conditions (Andrejczuk et al. 2010; Chandrakar et al. 2021; Christensen et al. 2023). Our choice of global model for this development is CESM since it is well documented and publicly available, and its single-column model (SCAM) version (Gettelman et al. 2019b) facilitates model development.

Another aspect of our approach is to use an observed case of deep convection [Midlatitude Continental Convective Clouds Experiment (MC3E)] as a testbed for model development. Aircraft observations of microphysical properties of convection and ground-based measurements (e.g., of precipitation and aerosol conditions) characterize the observed case. Thus, the degree of realism can be continuously evaluated as the model improvements are made.

The paper is structured as follows. Section 2 contains a description of the new microphysical scheme. This scheme is implemented in the deep convection parameterization using the single-column version of the NCAR Community Atmosphere Model, version 6, and initial forcing data are provided from the MC3E campaign data. Section 3 provides an overview of the MC3E campaign and experimental design. Section 4 shows the results from the validation of the scheme against

the observed case of convection and shows other aspects of the simulation using tagging tracers. The subsequent section shows results from sensitivity simulations of the microphysical scheme with respect to environmental conditions such as CCN and solid aerosols and to the inclusion of microphysical processes such as time dependence of INP activity. A summary and conclusions are presented in section 6.

2. Description of the new convective microphysical parameterization

a. Overview

With the current version of the SZ11 scheme, the ultimate problem is the lack of a realistic dynamical framework to provide a basis for treating the evolution of microphysical properties following the evolution of ascending cloudy parcels in deep updrafts, even if only in 1D (section 1). In reality, the actual number concentrations of cloud droplets and ice crystals result from the approach toward quasi-equilibrium during ascent, from sources and sinks of cloud particles, and from accretion onto the precipitation (Phillips 2022).

Consequently, for the present paper, the ZM convection scheme has been modified to create more realism of microphysical properties of the bulk plume, including new dependencies on the ambient aerosol conditions and in-cloud ascent. Specifically, the following changes have been made to the original ZM scheme (Zhang and McFarlane 1995; SZ11):

1) A modified time scale of 6 h is used in the closure scheme of the ZM scheme. The time scale of 6 h was chosen here based on an analysis of field observations of deep convection by Donner and Phillips (2003).
2) The triggering conditions for the convection have been modified to include convective inhibition (section 1).
3) SZ11 convective microphysics is replaced with our "new aerosol–cloud convection (ACC)" parameterization, which predicts the vertical profiles of microphysical properties in the plume by including a representative parcel that ascends in 1D at high resolution (time step of 0.025 s).
4) A new treatment of detrainment and entrainment is included in the ZM scheme.
5) The detrained cloud liquid, cloud ice, snow, rain, and graupel from convective outflow represent a source term for the prognostic hydrometeors for the large-scale cloud resolved on the global model grid.

Regarding the last point at detrainment, since graupel is not a prognostic variable in CAM6, the detrained graupel is added to the large-scale snow mass on the global model grid. In the original version, only the detrained cloud liquid and cloud ice were considered.

In the ACC scheme, the buoyancy-driven 1D Lagrangian parcel is initiated at the base of the bulk convective plume and ascends to the top of this plume. In this framework, the vertical profiles of all the cloud properties in the parcel, embedded in the bulk convective plume, are assumed to be representative of those of the deep convective clouds in the grid box. The new microphysical and dynamical evolution equations of the embedded Lagrangian parcel are described in sections 2d, 2d(4), and 2e.

The temperature and pressure of the ascending parcel follow the original equations for the bulk convective plume in the ZM convection scheme (appendix B) with interpolation to a much finer resolution. The initial vapor mass mixing ratio of the parcel is assumed to be the same as the environment at the starting level, and the liquid mass mixing ratio is set to zero initially at the base of the bulk convective plume. The initial vertical velocity of the parcel is set to 0.5 m s^{-1} in our parcel component. Then, the parcel is lifted by short variable steps of distance ($\delta z = w_{up} \times \Delta t$), according to the vertical velocity (section 2d) with a fixed time step of $\Delta t = 0.025$ s. This fine temporal resolution is also used for explicit treatment of diffusional growth of hydrometeors and continuous lateral entrainment. A coarser time step of 2.5 s is applied for all microphysical processes of coagulation in order to reduce computational expense.

The advanced representation of the microphysical processes is from the AC model, which is a 3D high-resolution cloud model with a mesoscale domain (Phillips et al. 2007, 2009, 2017a, 2018; Kudzotsa et al. 2016). It typically utilizes a horizontal resolution of 1 or 2 km. Phillips et al. (2017a,b, 2020) described the hybrid bin/bulk microphysical scheme of AC which involves five microphysical species (cloud liquid, cloud ice, rain, snow, and graupel/hail) and seven chemical species of aerosols (sulfate, sea salt, mineral dust, black carbon, soluble organics, primary biological particles, and nonbiological insoluble organics). The known and empirically quantified processes of cloud particle initiation for cloud liquid and cloud ice are represented. Several observed cases of various cloud types have been simulated by AC with validation of many cloud dynamical and microphysical quantities, including the ice concentration measured by aircraft (Phillips et al. 2017b; Waman et al. 2022, 2023; Gupta et al. 2023).

The new parcel model scheme resolves cloud microphysical processes in a similar way at each time step to assign the mass and number of hydrometeors in each species of cloud and precipitation (liquid, rain, ice, snow, and graupel/hail). The hydrometeors in the parcel are represented by the bulk prognostic variables when treating their advection and sedimentation. The emulated bin microphysical technique involves creating a temporary grid of size bins to discretize particle size distributions when treating the microphysical conversions among hydrometeors for coagulation and diffusional growth.

Also, graupel/hail is included as a new microphysical species in the ACC scheme. Graupel/hail forms either by riming of snow from the ice crystal process (Rogers and Yau 1989) or else by raindrop freezing followed by riming of frozen drops. Graupel/hail acquires its mass from the riming of supercooled cloud liquid and from raindrop freezing. Graupel/hail drives several key SIP processes because it falls fast and has a high collision kinetic energy (CKE) for fragmentation. Studies by Connolly et al. (2006) and Huang et al. (2017) show the impact of graupel/hail on the activation of the HM process. Other studies have shown the influential role of graupel/hail in the deep convective system (Bryan and Morrison 2012; Adams-Selin and Johnson 2013; Wu et al. 2013).

b. Particle size distribution

The size distribution of hydrometeors in each microphysical species is discretized with 33 size bins. The number distribution of hydrometeors (cloud liquid, cloud ice, rain, snow, and graupel/hail) is assumed to follow the gamma distribution (Phillips et al. 2007):

$$n(D_x) = n_{x,o} D_x^{p_x} e^{-\lambda_x D_x}. \quad (2)$$

Cloud liquid, cloud ice, snow, rain, and graupel/hail are represented by the subscript $x = w, i, s, r, g$, respectively. The term D_x is the equivalent spherical diameter, p_x is the shape parameter, λ_x is the slope, and $n_{x,0}$ is the intercept of the hydrometeors. The shape parameter p_w for water is 3.5, and for cloud ice, p_i is 1, based on the aircraft observations (Phillips et al. 2007). The shape parameter for rain is 2.5 (Ferrier 1994), and the slope parameter λ_x is determined using the mass and number bulk mixing ratios following Ferrier (1994). The shape parameter for graupel/hail p_g is unity. The shape parameter for snow is determined from the mass and number mixing ratios using a lookup table that accounts for the size dependence on bulk density and particle axial ratio. The slope parameters of graupel and snow are inferred with similar lookup tables that account for the size dependence of ice morphology (bulk density and shape). More details are given by Phillips et al. (2017b, 2020).

The mass in the smallest bin is prescribed according to an assumed smallest diameter:

$$m_{x,1} = \frac{\pi \rho_x D_{x,1}^3}{6}. \quad (3)$$

The subscript $x = w, I, s, r, g$ represents the cloud liquid, cloud ice, snow, rain, and graupel/hail, respectively. The term ρ_x is the bulk density of the hydrometeors corresponding to the subscript x, and it depends on the sizes for snow and graupel. Spherical equivalent diameters D_x of each bin are calculated from the prescribed mass, which is $D_{x,1}$ for the first bin. To prescribe the masses in all the bins, the mass of each bin is equal to that of the previous bin multiplied by a certain factor. During the simulation, the masses and sizes of the bins are fixed.

The bulk parameterization for cloud liquid and cloud ice is given by

$$n_x = \int_0^\infty n(D_x) dD_x / \rho, \quad (4)$$

where n_x is the number mixing ratio for cloud liquid, cloud ice ($x = W, I$). Thus,

$$q_x = \rho_x \frac{\pi}{6} \int_0^\infty D_x^3 n(D_x) dD_x / \rho, \quad (5)$$

where q_x is the mass mixing ratio for cloud liquid, cloud ice ($x = W, I$) and ρ_x is the bulk density of the particle (kg m^{-3}). The slope parameter λ_x is given by

$$\lambda_x = \left[\frac{\Gamma(4 + p_x) \rho_x \frac{\pi}{6} n_x}{\Gamma(1 + p_x) q_x} \right]. \quad (6)$$

Here, Γ is the gamma function. The bulk density of ice is $\rho_i = 900$ kg m^{-3}. For rain, snow, and graupel ($x = r, s, g$), the exponential size distribution by Lin et al. (1983) is assumed for bulk parameterization. Additional details are given by Phillips et al. (2007).

c. Aerosol distribution

The aerosol composition in the global model is represented by internally mixed sulfate modes (Aitken, accumulation, and coarse), sea–salt modes (Aitken, accumulation, and coarse), primary organic matter modes, secondary organic matter modes (Aitken and accumulation), black carbon, and mineral dust (Liu et al. 2016).

In the parcel model, aerosol particles are treated with a spectral bin approach, both in cloud and in the environment. In the environment of the parcel, the size distribution is discretized at each level by assuming the same average sizes of modes assumed by AC for each aerosol species and rescaling it to agree with the total mass of that species from the global model. The parcel uses the same system of size bins as in the environment and is initialized with the same aerosol size distribution as in the environment at the starting level near Earth's surface.

Following this approach from AC, the aerosol size distribution for each of the soluble and insoluble aerosol species consists of one or more modes, each conforming to a lognormal size distribution described by Pruppacher and Klett (2010):

1) Soluble species: There are two modes of sulfate [D_g at 0.03 and 0.18 μm in the planetary boundary layer (PBL), below 2 km altitude, and height-dependent formulas above] and similarly for secondary organic matter and sea salt (1 mode with D_g at 0.5 μm).
2) Insoluble species: There are modes for mineral dust (2 modes with D_g at 0.8 and 3 μm), black carbon (1 mode with D_g at 90 nm), insoluble nonbiological organic matter (1 mode with D_g at 90 nm), and primary biological organic matter (2 modes with D_g at 0.16 and 0.46 μm).

More details about these modes are given by Phillips et al. (2009). In the ascending parcel, the evolution of the number mixing ratio in each size bin for each chemical species of aerosols is predicted as described below.

d. Dynamical framework of the parcel theory

The ACC scheme is employed with an approximate method with two steps. This is done to represent the vertical velocity realistically with the weight of the cloud hydrometeors. In the first iteration of the microphysics, we get the provisional values of the cloud hydrometeors. These values are then used in the second iteration, to infer the vertical velocity with realism.

1) Triggering conditions

The convective available potential energy (CAPE) and convective inhibition (parameterization) are calculated by a new separate high-resolution integration for an adiabatic parcel without treatment of the microphysics, before the main

ascent of the parcel. The convection plume is triggered when there is significant CAPE (>70 J kg^{-1}) and CIN (<100 J kg^{-1}) that is not too large. The threshold for the CAPE is 70 J kg^{-1}, and for CIN, it is 100 J kg^{-1}. This contrasts with the previous treatment that omitted the CIN condition.

2) Detrainment rate

Previously, the ZM scheme used a vertical profile for updraft mass flux, with a certain formula for entrainment and with the detrainment flux calculated as a residual. The vertical profile of convective updraft mass flux relative to that at cloud base was constrained by an empirical statistical distribution of mass flux with respect to the entrainment rate of categories of plumes [Zhang and McFarlane (1995); Eqs. (3) and (4)]. The entrainment mass flux was determined by this statistical distribution which is constrained by buoyancy considerations [Zhang and McFarlane (1995); Eqs. (4), (5b), (A1), and (A2)]. The detrainment mass flux was inferred from the difference between the updraft mass flux and the entrainment mass flux.

However, in offline simulations of an observed case (MC3E), we found that the detrainment was predicted to be zero below the level of maximum entrainment rate. Arguably, this greatly underestimates the total outflow from convective plumes in most of the depth of the troposphere (section 1) because cloud modeling simulations show a deep layer of such outflow in mesoscale convective systems (MCSs) (Derbyshire et al. 2011). Consequently, we now changed this treatment of entrainment and detrainment by first specifying the detrainment flux from a recent formulation based on high-resolution cloud modeling (Derbyshire et al. 2011). The original estimate of the height dependence of the convective updraft mass flux in the ZM scheme is still applied here, because Zhang and McFarlane (1995) claimed that it is empirically realistic compared with field campaign observations. Finally, we improve the estimate of the entrainment mass flux by inferring the residual from the new detrainment mass flux and updraft mass flux. This approach has the advantage of guaranteeing a realistic deep layer of detrainment as is commonly known to produce the stratiform layer cloud shield uniting the convective cells in any MCS (Houze 2014).

In real deep convection, there are two types of detrainment: (i) turbulent exchange, which is usually assumed to occur with a constant rate (Bechtold et al. 2008) and is on a small scale (turbulent eddies are typically <100 m wide); and (ii) organized detrainment, which depends on the parcel buoyancy (Bechtold et al. 2008) and is on a larger scale (e.g., a few kilometers). de Rooy et al. (2013) highlight the role of detrainment in determining the vertical structure of real convective clouds.

Specifically, the new detrainment rate from the cloud modeling by Derbyshire et al. (2011) is formulated as follows. The convective outflow is represented by two components, namely, turbulent detrainment and organized detrainment (ECMWF 2021). The turbulent detrainment follows Bechtold et al. (2008), and the organized detrainment follows the new scheme from Derbyshire et al. (2011). Therefore,

$$D_u = D^{(1)}_{\text{deep}} + D^{(2)}_{\text{deep}}, \tag{7}$$

where D_u is the total detrainment rate, while $D^{(1)}_{\text{deep}}$ is turbulent detrainment for deep convection and $D^{(2)}_{\text{deep}}$ is organized detrainment by loss of buoyancy. The term $D^{(1)}_{\text{deep}}$ is given as follows:

$$D^{(1)}_{\text{deep}} = \delta^{\text{up}} M_{\text{up}}(1.6 - \text{RH}). \tag{8}$$

Here, $\delta^{\text{up}} = 0.75 \times 10^{-4}$ m^{-1}, RH is the fractional relative humidity in the environment, and M_{up} is updraft mass flux (kg m^{-2} s^{-1}) from the original ZM scheme as noted above. The term $D^{(2)}_{\text{deep}}$ is given as follows:

$$D^{(2)}_{\text{deep}} = -(M_{\text{up}}) R_{\text{det}} \left(\frac{\partial \ln \Theta'_v}{\partial z} \right)_*. \tag{9}$$

Here, $R_{\text{det}} = 0.6$ is the compensation parameter (dimensionless) and $[(\partial \ln \Theta'_v)/\partial z]_*$ is the rate of loss of buoyancy. The term Θ'_v is the effective buoyancy (dimensionless), which is the difference in virtual effective temperature defined below [Eq. (13)]. The term $R_{\text{det}} \times [(\partial \ln \Theta'_v)/\partial z]_*$ is the fractional rate of loss of buoyancy.

The functional form of the entrainment rate is given by

$$E_{\text{up}} = \frac{\partial M_u}{\partial z} + D_u, \tag{10}$$

where E_{up} is the entrainment rate, M_u is the updraft mass flux, and D_u is the detrainment rate.

3) Vertical velocity

The vertical velocity $w_{\text{up}}(z)$ profile for the parcel is obtained from the integration of the kinetic energy vertical gradient in a manner similar to Simpson and Wiggert (1969):

$$\frac{\partial K_{\text{up}}}{\partial z} = \frac{-\mu_{\text{up}}}{M_{\text{up}}}(1 + \beta C_d) 2K_{\text{up}} + \frac{1}{f(1+\gamma)} g \frac{T_{v,\text{up}} - \overline{T}_v}{\overline{T}_v}, \tag{11}$$

with

$$K_{\text{up}} = \frac{w^2_{\text{up}}}{2}, \tag{12}$$

where K_{up} is the kinetic energy of the updraft, μ_{up} is the mixing coefficient equal to the larger of the entrainment or detrainment, M_{up} is the updraft mass flux, g is gravitational acceleration, and $T_{v,\text{up}}$ and $\overline{T}_v$ are the virtual temperatures of the updraft and the environment, respectively. The term $\beta = 1.875$, $\gamma = 0.5$ is the virtual mass coefficient, and $C_d = 0.506$ is the drag coefficient (Simpson and Wiggert 1969), and $f = 2$ because flow is turbulent (Cheng et al. 1980).

The ascent of the parcel is dependent on the temperature, weight of the condensate (cloud liquid, rain, cloud ice, graupel,

and snow), gravity, momentum drag, and entrainment/detrainment mass flux of the environment.

When inferring the vertical velocity w_{up} of the parcel in the plume using Eq. (12), we artificially threshold it everywhere below the level of free convection (LFC), to ensure that it never decreases with height and is never less than 0.5 m s^{-1}. During the convection, this implicitly represents the lifting of the parcel up to the LFC despite being negatively buoyant. The LFC is evaluated from our CAPE and parameterization calculation, as noted above.

The use of Eqs. (11) and (12) is consistent with how buoyant convection converts gravitational potential energy to kinetic energy of ascent. For the effective buoyancy of the parcel $g(T_{v,up} - \overline{T}_v)/\overline{T}_v$, the effective virtual temperature is calculated by accounting for the weight of the condensate as

$$T_{v,up} = T_v(1 + 0.608q_v - q_c - q_i - q_s - q_r - q_g). \quad (13)$$

The variables are defined in the Table A1 in appendix A.

4) Evolution equation of aerosol and microphysical species

We numerically integrate the continuous entrainment equations with the same fine time step noted above (0.025 s), during the entire ascent of the parcel from ground to maximum cloud top. Hence,

$$\frac{DX}{Dt} = -E_u(X - X_{env}) + \sum S_X, \quad (14)$$

where X signifies any conserved variable such as mass and number mixing ratio of cloud liquid, cloud ice, rain, snow, graupel/hail, and actual number mixing ratio for each size bin of the aerosols in any given chemical species (e.g., sulfate, dust, and sea salt). The term X_{env} represents the environmental variable corresponding to X at the same altitude. The term E_u is the entrainment rate with units of inverse second (s^{-1}), and S_X signifies the source/sink term corresponding to subscript X.

5) Tagging tracers

The components of mass and number concentration of cloud ice from each process of ice initiation (heterogeneous nucleation, homogeneous freezing, and SIP) are tracked using passive prognostic variables. These tagging tracers are updated based on any relevant microphysical processes and do not alter the simulation in any way. Information from the tagging tracers is used to analyze the contribution from different sources of ice to total cloud-ice number concentration. A similar approach is used to track the contribution from secondary droplets (the cloud droplets initiated from in-cloud droplet activation).

e. Microphysical processes of initiation of hydrometeors

In the public CAM6 version of the global model, the microphysical properties of deep convective clouds are now represented with the new 1D parcel scheme that provides an adequate dynamical framework for treating the microphysical evolution during ascent.

1) Cloud droplet activation

The aerosol species described in section 2c act as CCN to initiate cloud droplets at cloud base and in cloud. The initiated cloud droplets then grow by condensation.

(i) Cloud-base droplet activation

Soluble aerosols initiate cloud droplets when the supersaturation is positive, forming a cloud base. The cloud droplet nucleation scheme by Ming et al. (2006) is implemented (appendix C, section a).

(ii) In-cloud droplet activation

The activation of droplets by soluble aerosol species and insoluble species, which may be coated with soluble material, in cloud follows the κ-Kohler theory (Petters and Kreidenweis 2007). Equation (14) is used to predict the evolution of vapor mixing ratio at every fine time step during the ascent, and the corresponding ambient supersaturation with respect to liquid is compared with the critical supersaturation for activation in each size bin for each aerosol species. This critical value depends on the volume-weighted average of hygroscopicity κ among internally mixed components of each aerosol particle.

As noted above, the evolution of aerosol number in each bin is predicted in the parcel also by Eq. (14), with lateral entrainment of environmental aerosols at each level. When the critical supersaturation is exceeded, then the aerosols are converted to cloud droplets. In this way, effects on the cutoff size of the aerosol size distribution from cloud-base activation (Ochs 1978; Pinsky and Khain 2002) and from lateral entrainment of environmental aerosols (Fridlind et al. 2004), determining the occurrence of in-cloud activation, are realistically simulated.

2) Heterogeneous ice nucleation

The empirical parameterization (EP) of heterogeneous ice nucleation by multiple chemical species of aerosol, developed by Phillips et al. (2013, 2008), is implemented (appendix C, section b). The EP is based on field measurements of aerosol conditions and INP activity from the Ice Nuclei Spectroscopy (INSPECT) campaigns (DeMott et al. 2003; Richardson et al. 2007) and also is informed by laboratory measurements. Recently, time dependence of INP activity was represented in the EP framework following the laboratory observations by Jakobsson et al. (2022).

Time dependence

Jakobsson et al. (2022) performed laboratory experiments to quantify the time dependence of freezing for immersed INPs from the atmospheric aerosol samples. They observed an increase in concentrations of active INPs by 70%–100% over periods of 2–10 h. Jakobsson et al. (2022) proposed a method to include time dependence in numerical models using the framework of the EP, incorporating the laboratory results.

The age of the parcel $\tilde{t}$ since entering the subzero degree Celsius parts of the cloud is estimated by the exponential decay of a passive tracer Q following a similar continuous entrainment equation [Eq. (14)], including effects from mixing. This time taken determines the amplification of the INP activity. However,

$$\frac{DQ}{Dt} = \begin{cases} -Q/\tau_Q, & T < 0°\text{C and IWC} > 10^{-6}\text{kg m}^{-3} \\ 0 \text{ kg m}^{-3}, & \text{otherwise} \end{cases}, \tag{15}$$

where $Q = Q_0 = 1$ kg^{-1}, everywhere outside the glaciated part of the cloud both in the environment and in the parcel. The term $\tau_Q = 1800$ s is an arbitrary relaxation time. The analytical solution of Eq. (15) is given as

$$\tilde{t} \approx -\tau_Q \ln(Q/Q_0). \tag{16}$$

The term $\tilde{t}$ is then used to determine the temperature shift in the solid aerosol species $\Delta\tilde{T}_X$ as follows:

$$\Delta\tilde{T}_X = -A_X \tilde{t}^{-\beta_X}, \tag{17}$$

where A_X and β_X are the fitting constants corresponding to subscript X with values provided in Jakobsson et al. (2022; Table 6). More details of the method are presented in Waman et al. (2023) and Jakobsson et al. (2022).

3) Homogeneous ice nucleation

The freezing of supercooled cloud droplets and rain occurs at about −35° to −37°C depending on drop size, following Phillips et al. (2007, 2009). Homogeneous aerosol freezing is neglected here because it happens in weak ascent and not in the convective updraft.

4) Hallett–Mossop/Rime splintering

The Hallett–Mossop process (Hallett and Mossop 1974) follows Phillips et al. (2007) and Kudzotsa et al. (2016) (appendix C, section c). There is an ambiguity regarding the existence of the HM process in modern laboratory experiments (Hartmann et al. 2023), although aircraft observations by Harris-Hobbs and Cooper (1987) were consistent with their existence in hundreds of warm-based convective clouds over the United States. Other field experiments by Crosier et al. (2011) and Lasher-Trapp et al. (2016) observed rimed ice particles in the regions ~5°C and theorized this rimed ice could be produced from the HM process of rime splintering.

5) Breakup in ice–ice collision

The formulation by Phillips et al. (2017a) is implemented, which uses energy conservation to determine the number of secondary fragments from collisions among ice particles. The scheme is based on temperature, size, ice morphology, and CKE for each permutation of size bins for colliding particles in any pair of microphysical species. Recent field observations of the fragmentation of snow by Gautam (2022) support the scheme.

6) Raindrop freezing fragmentation

An empirical formulation developed by Phillips et al. (2018) that treats raindrop freezing fragmentation in two modes, namely, quasi-spherical (mode 1) and nonspherical freezing modes (mode 2), is implemented.

- Mode 1: Secondary ice is produced when a supercooled rain/drizzle drop (0.05–5 mm in diameter) either collides with a less massive ice particle or freezes heterogeneously when an immersed INP activates.
- Mode 2: Collision of a supercooled raindrop with a more massive ice particle produces secondary ice from the emission of secondary droplets (e.g., from a splash).

Recent laboratory observations by James et al. (2021) have measured the probability of any secondary droplet freezing for mode 2 to form ice. Based on this study, the probability is now set to 0.3 in the scheme.

f. Microphysical processes of growth of hydrometeors

1) Condensational growth of cloud droplets

The equations used for the condensation growth process are from Rogers and Yau [1989; their Eqs. (9.4) and (7.18)]. We use the emulated bin microphysical approach (section 2b) to calculate the rate of change of mass of each droplet in any bin. Here,

$$\frac{dm(j)}{dt} = \frac{4\pi r(j) s_w}{\left[\left(\frac{L_v}{R_u T} - 1\right)\frac{L_v}{KT} + \frac{R_v T}{e_w(T) D}\right]}, \tag{18}$$

where j is the index for the bin, $r(j)$ is the radius of the cloud droplet for the jth bin, L_v is the latent heat of vaporization, R_v is the gas constant for water vapor, T is the temperature of the parcel, K is the coefficient of thermal conductivity of air, $e_w(T)$ is the saturation vapor pressure relative to water, s_w is the supersaturation with respect to water, and D is the molecular diffusion coefficient.

2) Vapor growth of ice

The crystal growth rate given in Rogers and Yau [1989; their Eq. (9.4)] is implemented using the emulated bin approach. Therefore,

$$\frac{dm(j)}{dt} = \frac{4\pi r(j) s_i}{\left[\left(\frac{L_s}{R_v T} - 1\right)\frac{L_s}{KT} + \frac{R_v T}{e_i(T) D}\right]}, \tag{19}$$

where j is the index of the bin, $r(j)$ is the radius of the cloud ice for the jth bin, L_s is the latent heat of sublimation, s_i is the supersaturation with respect to ice, and $e_i(T)$ is the saturation vapor pressure relative to ice.

3) Autoconversion of cloud water to rain

Autoconversion of cloud water by rain uses the formulation by Kogan (2013) for deep convection (appendix C, section d).

4) AUTOCONVERSION OF CLOUD ICE TO SNOW

The conversion of cloud ice to snow follows Ferrier (1994), with modifications described in Kudzotsa et al. (2016) (appendix C, section e).

5) ACCRETION OF CLOUD WATER BY RAIN

The accretion of cloud water is treated using the turbulent enhancement scheme developed by Benmoshe and Khain (2014), with modifications described in Kudzotsa et al. (2016). The accretion of cloud water by rain depends on the collection efficiencies [appendix C, section g(1)] that depend on the size or fall speed, air density, and sometimes temperature for each permutation of size bins for colliding microphysical species.

6) AUTOCONVERSION OF SNOW TO GRAUPEL/HAIL

Graupel/hail is formed by heavy riming of snow, and this conversion is treated with an assumed dependency of rime fraction on size (Phillips et al. 2017b) (appendix C, section f).

7) AGGREGATION PROCESSES

The interactions between cloud ice, graupel/hail, and snow lead to the formation of aggregates (Table 1) and fragments described in section 2e(5). The rate of collision is computed from the collision efficiency and the volume swept out by the interacting particles (Kudzotsa et al. 2016), applying the continuous collection equation to each permutation of bins of colliding species. The collisions can cause the breakup of particles or aggregation. The sticking efficiency follows Phillips et al. (2015) (appendix C, section c). Particles with sizes < 0.3 mm are added to cloud ice, and added to snow and graupel, otherwise. Equations (C12) and (C13) give the rate of change of mass mixing ratio and number concentration per unit time.

g. Fallout of rain and graupel/hail

Bulk microphysical formulas are used to evaluate the number-weighted and mass-weighted fall velocities V of number and mass, respectively, for rain (Ferrier 1994). At every time step, each prognostic variable is reduced by the fraction $V\Delta t/H$, where $H = 1500$ m is the depth of the parcel.

The fallout of graupel also utilizes this fractional reduction in time step, but the number-weighted and mass-weighted fall speeds are evaluated numerically from the size dependencies of bulk density and shape in each bin and from the related size distribution parameters μ and λ (section 2b).

3. Validation of the new microphysical scheme with the MC3E campaign

a. MC3E campaign

The MC3E campaign was conducted over the Atmospheric Radiation Measurement (ARM) Southern Great Plain (SGP) with Central Facility (CF) located at 36.695°N, 97.485°W and 20 extended facilities covering a region of about 150 km. The campaign was carried out from 2 April to 6 June 2011, with data collected from airborne and ground-based observations (Jensen et al. 2016). A variety of mesoscale cloud systems were sampled.

1) 11 MAY 2011 MCS

We simulated the MCS case observed on 11 May 2011. The organized severe convection was triggered by a surface cold front advancing through the Texas–Oklahoma Panhandle (Jensen et al. 2016), and the system moved northeastward. The deep convective system was already mature with a trailing stratiform shield when passing over the CF. Figure 1 presents the initial atmospheric profile for 0000 UTC 10 May 2011, with a high CAPE of 3515 J kg^{-1}. The lifting condensation level (LCL) is at 827 hPa. The cloud base is at 18°C with a mean sea level (MSL) altitude of 315 m.

2) AIRBORNE MEASUREMENT

Flights by the National Aeronautics and Space Administration (NASA) ER-2 and the University of North Dakota (UND) Cessna Citation II aircraft were utilized. The NASA ER-2 worked as the Global Precipitation Measurement (GPM) core-satellite sampling simulator. The Citation II carried meteorological instruments, including cloud microphysical, precipitation, and total liquid water content probes, as described in Table 2. The emphasis of the aircraft sampling was on measurements of ice-phase hydrometeors at altitudes between the melting level and the cloud top (~4–13 km). The main focus of the Citation II aircraft was to measure the ice-phase hydrometeors in the stratiform outflow from convection. The cloud droplet probe (CDP) measured the size and concentrations of droplets and also the liquid water content (LWC). LWC was also measured by the King hot-wire liquid water content (KING) and Nevzorov probes. Ice concentrations were measured with the 2D cloud imaging probe (2DC), cloud imaging probe (CIP), and high-volume precipitation spectrometer, version 3 (HVPS-3). The resolution of the 2DC and CIP probes was about 30 μm per pixel, resulting in their inability to reliably assess particle size and concentration in the size range of 50–200 μm. Also, the 2DC and HVPS-3 probes had shattering-corrected tips, deflecting artificial fragments of ice from impact with the probe out of the laser beam (Korolev et al. 2011), whereas the CIP probe did not. The coarse resolution and shattering effect make it unreliable to use the observations by these probes in the size range of 50–200 μm. The combine spectrum (COMB) combines the particle size distribution from the HVPS-3 and 2DC (or CIP). The method described by Field et al. (2006) was followed to reduce the contribution of shattered ice particles in the aircraft data. The validation plots are generated by including only ice particles larger than 0.2 mm in maximum dimension for both observations and simulations.

3) GROUND-BASED MEASUREMENTS

During the MC3E campaign, large-scale advective tendencies of heat and moisture and the surface heat and moisture fluxes were derived by Xie et al. (2014) using constrained variational analysis. 16 rain gauge pairs and 18 autonomous particle size and velocity disdrometers were set up at the SGP site within a 6-km radius of the CF. The CCN counter measured the CCN number concentration there (Jefferson 2011; Uin and Enekwizu 2024).

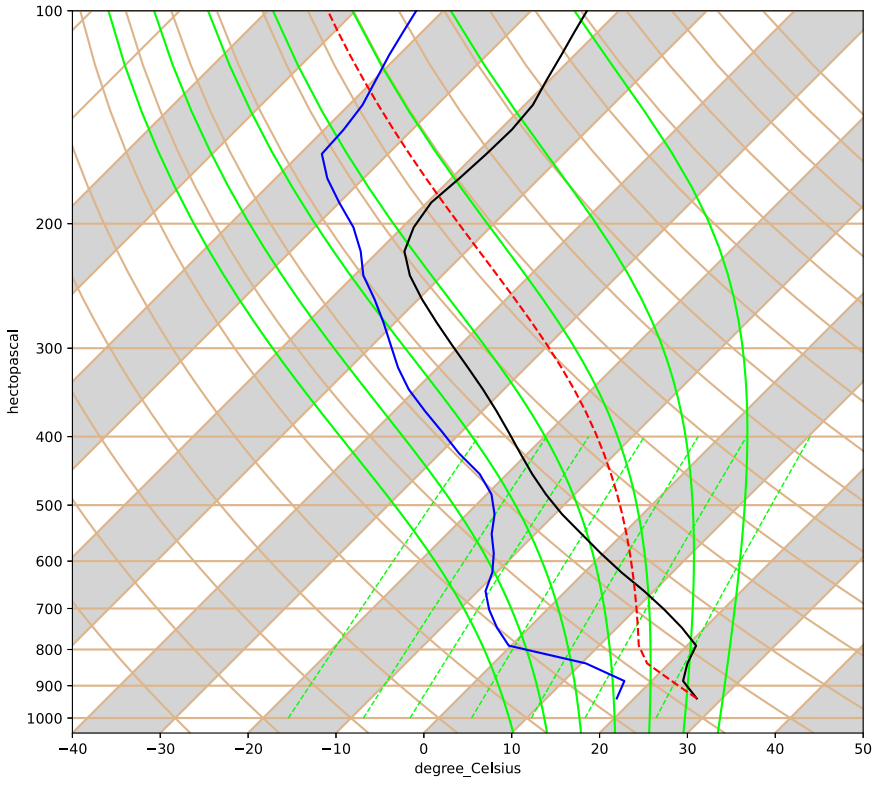

FIG. 1. A skew T–log$P$ diagram showing the atmospheric profiles of temperature (solid black line) and dewpoint temperature (solid blue line) for the initial simulation time of 0000 UTC 10 May 2011.

b. *Model and experimental design*

CESM consists of different component models including components for the land surface, atmosphere, ocean, sea ice, and biogeochemistry. These components interact with each other in the simulations, representing to a degree some of the complex feedbacks and processes occurring in Earth system. CESM has been applied to study atmospheric phenomena over a wide range of time scales, from past to future.

We have used the single-column version of the CESM for our development of convection parameterization. The scheme was originally implemented in CAM6 as described by Zhang and McFarlane (1995). We replaced the microphysical treatment of SZ11 with the scheme presented in the paper. We have altered the treatment of convective dynamics in the bulk plume of the convective parameterization also.

We simulated the event from 10 to 12 May 2011 with a global model time step of 20 min in SCAM. The intensive observation period (IOP) of the MC3E has yielded a large-scale advective forcing for running models that are evaluated by Xie et al. (2014) covering the campaign period at 3-hourly time intervals. It includes surface fluxes and tendencies of advection of temperature and moisture.

TABLE 1. Collisional interactions between the three microphysical species of ice. Columns are the collecting particles, and rows represent the collected particles, where m_g is the mass of any graupel/hail particle and m_s is the mass of any snow particle.

Ice particles	Cloud ice (particles < 0.3 mm)	Snow (aggregates/crystals > 0.3 mm)	Graupel/hail (>0.3 mm)
Cloud ice	Growth of cloud ice by aggregation	Growth of snow by aggregation	Collection of ice by graupel/hail; secondary cloud ice is initiated by breakup of rimed particles
Snow	—	Secondary cloud ice or snow is initiated by breakup	Growth of graupel by aggregation ($m_s > m_g$); secondary cloud ice or snow is initiated by breakup
Graupel/hail	—	Growth of snow by aggregation ($m_s > m_g$); secondary cloud ice or snow is initiated by breakup	Secondary cloud ice is initiated by breakup

TABLE 2. Meteorological instruments carried on Citation II aircraft.

Instrument	Range
Cloud imaging probe (CIP)	0.025–1.5 mm
2D cloud imaging probe (2DC)	0.03–1.0 mm
High-volume precipitation spectrometer, version 3 (HVPS-3)	0.15–19.2 mm
Cloud droplet probe (CDP)	2–50 μm
King hot-wire liquid water content probe	0.01–5 g m^{-3}
Nevzorov probe	0.03–3 g m^{-3}

Aerosol concentrations are initialized based on the Goddard Chemistry Aerosol Radiation and Transport (GOCART) global model (Chin et al. 2000). These were rescaled near the ground using the averaged coincident measurements of aerosol mass mixing ratios for the time period 9–12 May 2011 from the Interagency Monitoring of Protected Visual Environments (IMPROVE). The same rescaling factor is applied at all levels aloft.

In the simulation (referred to as ACC_24), our ACC parameterization scheme is included in the CAM6. Results are validated against aircraft data from the MC3E campaign. For the purpose of the present comparison, convective ascent is defined to be where the vertical velocity is greater than 3 m s^{-1} both in the aircraft observations and in the averaging of the ACC_24 simulation. This threshold was selected because the aircraft flight strategy involved preferential sampling of trailing stratiform clouds and weak convective ascent, whereas the bulk plume represents a stronger convective ascent. The tagging tracers have been conditionally averaged over the convective cloudy updrafts ($w_{up} > 3$ m s^{-1}) over the entire simulation period.

To avoid the bias from the shattering of ice on the probes as noted above [section 3a(2)], ice particles with sizes greater than 0.2 and 1 mm are plotted, for both the observation data and the model results.

4. Results from simulating the MC3E storm with ACC parameterization

a. *Validation of the microphysical parameterization*

The ACC_24 simulation of the MC3E storm (section 3a) with the SCAM version of the CESM running the ACC scheme (section 2e) is compared with coincident aircraft observations [section 3a(2)] and with ground-based measurements [section 3a(3)].

Figure 2a shows that the observed precipitation rate has two peaks, namely, a weak first peak at 1800 UTC 10 May 2011 and a strong second peak from deep convection at 1800 UTC 11 May 2011.

Figure 2a shows the simulated precipitation peaks occur at 0100 and 2300 UTC 11 May, a few hours late. The maximum intensity in surface precipitation rate of the stronger peak is predicted to be 6 mm h^{-1}, which is about 40% higher than the observed peak. Inevitably, this phenomenon for the simulated precipitation to fall too suddenly and too late, yet with

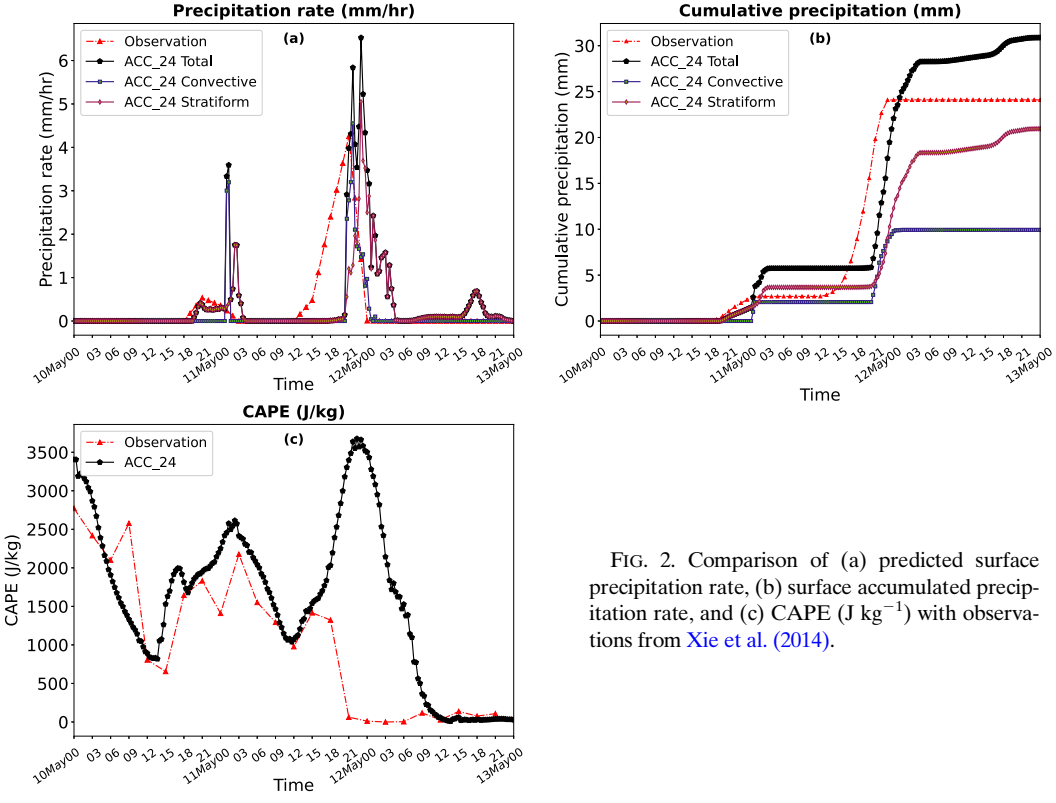

FIG. 2. Comparison of (a) predicted surface precipitation rate, (b) surface accumulated precipitation rate, and (c) CAPE (J kg^{-1}) with observations from Xie et al. (2014).

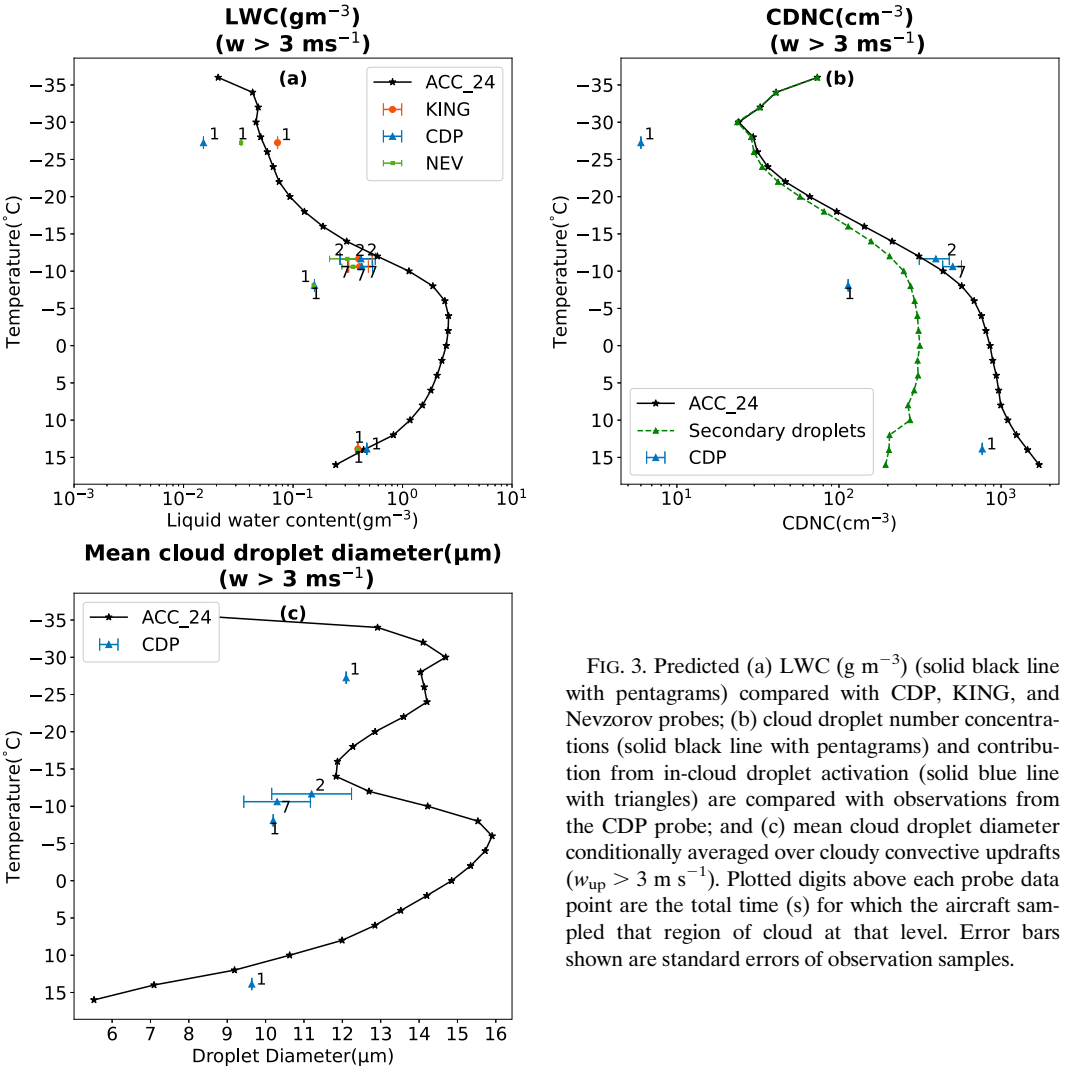

FIG. 3. Predicted (a) LWC (g m^{-3}) (solid black line with pentagrams) compared with CDP, KING, and Nevzorov probes; (b) cloud droplet number concentrations (solid black line with pentagrams) and contribution from in-cloud droplet activation (solid blue line with triangles) are compared with observations from the CDP probe; and (c) mean cloud droplet diameter conditionally averaged over cloudy convective updrafts ($w_{up} > 3$ m s^{-1}). Plotted digits above each probe data point are the total time (s) for which the aircraft sampled that region of cloud at that level. Error bars shown are standard errors of observation samples.

eventually a realistic total surface accumulation, is to be expected of such conventional convection parameterizations with simplified dynamics and only one bulk plume, which removes precipitation instantly from the model. In reality, the 3D overturning in the boundary layer and the density currents create the onset of deep convection, and these phenomena cannot be treated directly here.

Figure 2b shows that the surface-accumulated precipitation of the ACC_24 simulation differs from that observed by only about 30% throughout the simulation. The stratiform precipitation is seen to be a major contributor to the cumulative surface precipitation as found also in high-resolution 3D simulations by Gupta et al. (2023).

Moreover, the predicted maximum of CAPE in Fig. 2c before the first peak of the precipitation is 2400 J kg^{-1} and at the second peak is 3400 J kg^{-1}. The predicted CAPE is higher than the observations by about 50% and a factor of 2 for the first and second peaks, respectively. This is an inevitable consequence of convection being treated with a single bulk plume, with convection starting late and intensifying too suddenly, as noted above. The observed CAPE is averaged over the global model gridbox area (about 150 km wide), whereas the CAPE related to the convection in the model must be more local and with extreme values, in view of the strong spatial variability of the CAPE on the convective scale (Donner et al. 2001). Such variability cannot be treated in the present scheme.

The cloud microphysical properties in deep convective ascent are shown in Figs. 3–5 and are validated against the aircraft data. The cloud droplet properties of droplet diameter, CDNC, and LWC in Fig. 3 are comparable with the observations, each prediction differing from corresponding observations by less than the differences between these observations at adjacent levels. The simulated cloud base is at about 16°C.

In Fig. 3a, above the freezing level, where most of the LWC observations occur, the predicted LWC differs from the observations by less than a factor of 2. Similarly, the average droplet diameter agrees with the observations to within about ±20%.

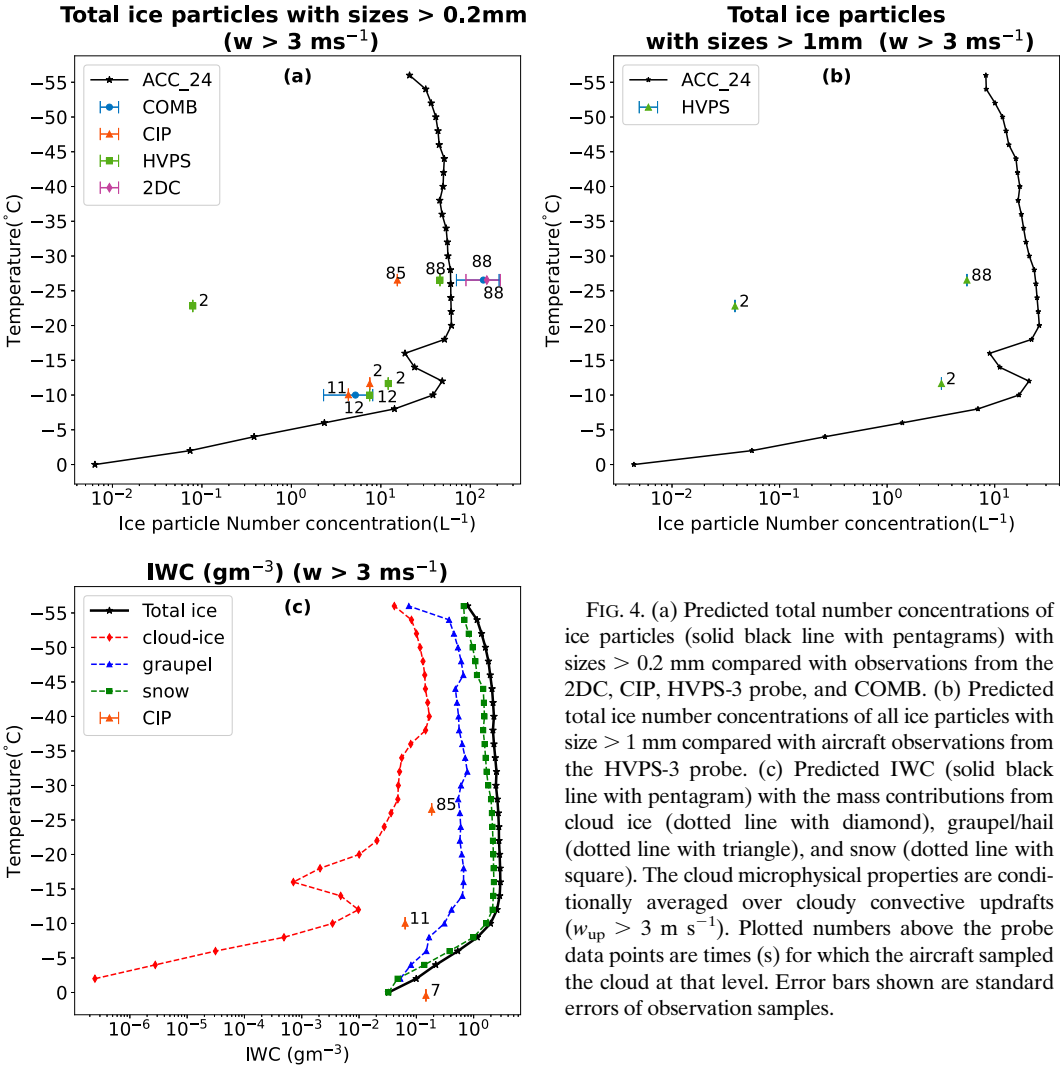

FIG. 4. (a) Predicted total number concentrations of ice particles (solid black line with pentagrams) with sizes > 0.2 mm compared with observations from the 2DC, CIP, HVPS-3 probe, and COMB. (b) Predicted total ice number concentrations of all ice particles with size > 1 mm compared with aircraft observations from the HVPS-3 probe. (c) Predicted IWC (solid black line with pentagram) with the mass contributions from cloud ice (dotted line with diamond), graupel/hail (dotted line with triangle), and snow (dotted line with square). The cloud microphysical properties are conditionally averaged over cloudy convective updrafts (w_{up} > 3 m s^{-1}). Plotted numbers above the probe data points are times (s) for which the aircraft sampled the cloud at that level. Error bars shown are standard errors of observation samples.

The role of in-cloud droplet activation is revealed by the tagging tracer shown in Fig. 3b (green dashed line with triangles). Above the −5°C level, most of the cloud droplets are from in-cloud droplet activation. The predicted CDNC at about −10°C differs from the observations by only 10%. The component of CDNC from in-cloud droplet activation peaks at −2°C and is a source of cloud droplets in the regions above cloud base. The CDNC reduces with height because of lateral mixing and dilution with the environment and microphysical sinks of cloud droplets.

In Figs. 3c and 3b below the freezing level, the predicted mean size of cloud droplets increases with height, with a reduction in the CDNC. Additionally, a larger mean droplet size increases the likelihood of precipitation, as the droplets can coalesce with a higher collision efficiency and greater differences in fall speeds, forming larger drops that can grow and fall as rain. The predicted LWC and CDNC are slightly higher than observations at certain levels because the Citation II aircraft flew preferentially in the trailing stratiform region of the MCS system (Jensen et al. 2016) and did not sample as comprehensively the convective cores.

Figure 4 demonstrates that the predicted microphysical properties of ice are in good agreement with the observational probe data (2DC, CIP, and HVPS-3) in the convective ascent.

Figure 4a shows the predicted total ice particle concentration for ice particles with sizes greater than 0.2 mm has a good agreement with the observations. At about −10° and −11°C levels where observations are present, these predicted ice number concentrations differ from observations by a factor of about 10. At −15°C, the results are in good agreement with the observations.

Figure 4b predicted total ice particle number concentration for ice particles with sizes greater than 1 mm is of the same order as the observations at all levels where observations are present. The predicted total ice particle concentrations differ from the observations by about a factor of 4 or 5.

Figure 4c shows that the predicted ice water content (IWC) shows that snow and graupel mass is the major source of ice mass in the simulated convective clouds, also seen in Fig. 5f.

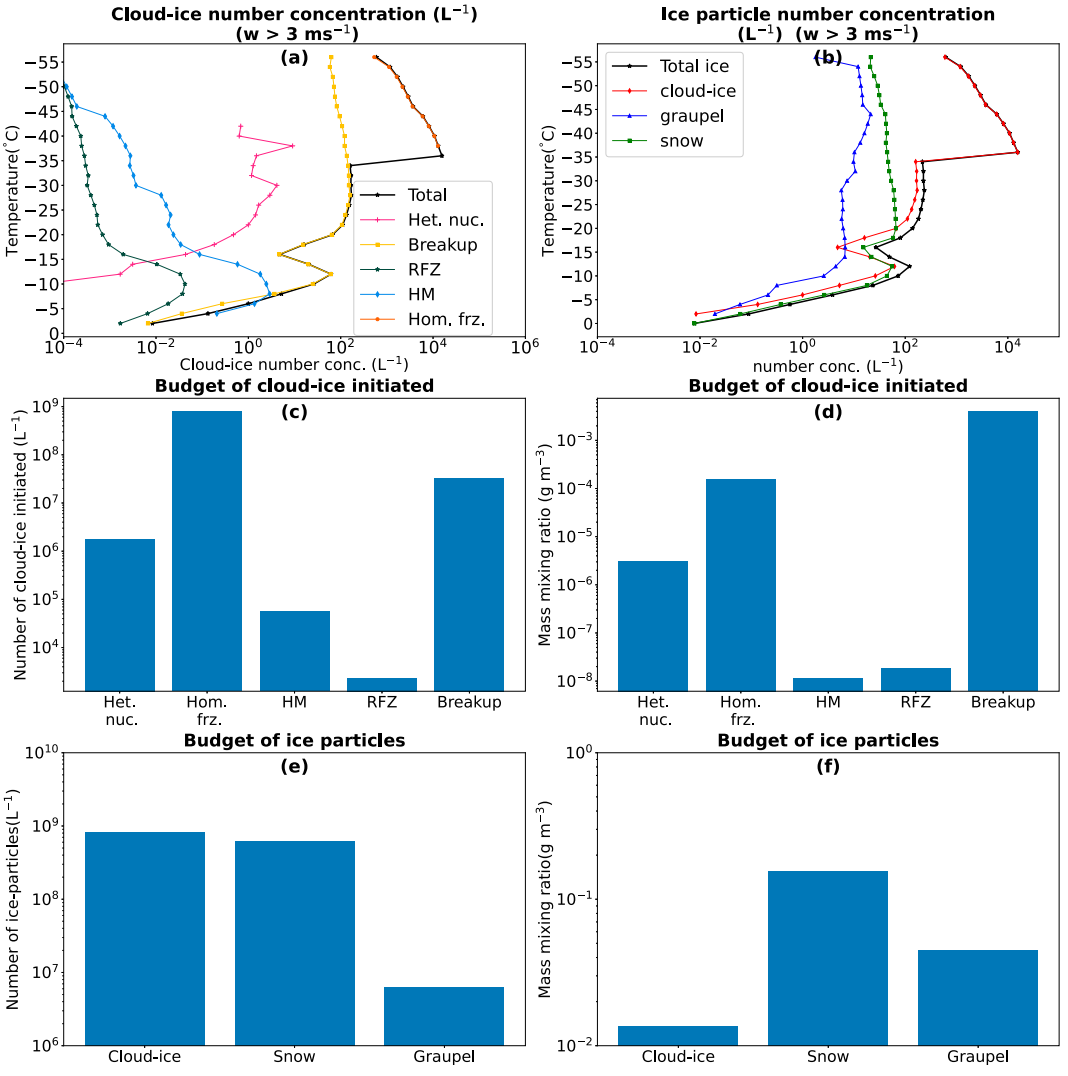

FIG. 5. (a) Comparison of the predicted total number of cloud ice from the SIP mechanism in the simulation compared with predicted total cloud ice.(b) The contributions from cloud ice (dotted line with diamond), graupel/hail (dotted line with triangle), and snow (dotted line with square) are plotted, as well as total ice (solid line with pentagram). Bar plot for the (c) budgets of the number of cloud-ice particles and (d) budget of the mass mixing ratio of cloud-ice particles initiated from heterogeneous ice nucleation ("Het. nuc."), homogeneous freezing ("Hom. frz."), breakup in ice–ice collisions ("Breakup"), raindrop freezing fragmentation ("Rfz"), and HM process. Bar plot of the (d) budgets of the number and (e) budget of the mass mixing ratio of cloud ice, snow, and graupel particles initiated in the cloud for the ACC_24 simulation. The cloud microphysical properties are conditionally averaged over cloudy convective updrafts ($w_{up} > 3$ m s^{-1}).

Gettelman et al. (2019a) also observed in their offline kinematic driver test that snow and graupel contribute significant ice mass.

b. *Further analysis of ACC_24 simulation*

Tagging tracers in the ascending parcel are useful to identify and trace the sources of the cloud ice at each level in the simulation of the bulk convective plume. This information provides insight into the complex interactions between the cloud hydrometeors to produce cloud ice. The prevalence of SIP mechanisms in natural clouds has been highlighted in past studies as reviewed by Field et al. (2017). Specifically, tagging tracers have been included to track ice particles from these sources of ice production [section 2d(5)]:

- Homogeneous freezing
- Heterogeneous nucleation
- HM rime splintering
- Breakup in ice–ice collisions
- Fragmentation by raindrop freezing

Figure 5a shows that in the mixed-phase region, breakup in ice–ice collisions is the most prolific of all pathways of ice

TABLE 3. List of the sensitivity simulations.

Name of simulation	Description
ACC_24	Includes the ACC parameterization scheme with all the processes
SZ11	SCAM run with the parameterization scheme by SZ11
Time dependence	Time dependence of the INP is included in the EP of the ACC_24 run
High CCN	Soluble aerosol species are changed by a height-dependent factor that decreases linearly from 10 at ground toward unity at 11-km altitude from the ACC_24 run
Low CCN	Soluble aerosol species are changed by a height-dependent factor that increases linearly from 0.1 at ground toward unity at 11-km altitude from the ACC_24 run
High INP	Solid aerosol species are changed by a height-dependent factor that decreases linearly from 10 at ground toward unity at 11-km altitude from the ACC_24 run
Low INP	Solid aerosol species are changed by a height-dependent factor that increases linearly from 0.1 at ground toward unity at 11-km altitude from the ACC_24 run
No HM	HM process is inactive in the ACC_24 run
No-ice–ice collisional breakup	The breakup in ice–ice collision process is inactive in the ACC_24 run
No-raindrop freezing fragmentation	The raindrop freezing fragmentation process is inactive in the ACC_24 run
No SIP	All three SIP mechanisms are inactive in the ACC_24 run

initiation. The HM process of rime splintering is predicted to be active in the region of −3° to −8°C level, but the simulated number of ice splinters generated is not significant compared to the other SIP mechanisms because the mean droplet size in this case is too small. The raindrop freezing fragmentation is minimal, being less prolific than heterogeneous ice nucleation, due to little coalescence f and the mean droplet diameter being less than 15 μm at all subzero levels (Fig. 3c). The breakup in ice–ice collisions is predicted to be dominant because of its positive feedback with the riming of snow from fragments to become graupel/hail, yielding snow–graupel collisions. It contributes about 99% of the total ice number concentration throughout most of the mixed-phase region. This is consistent with high-resolution cloud modeling results (Waman et al. 2022, 2023). In short, the ACC scheme predicts that at all subzero levels below the −36°C level, the ice multiplication processes are predicted to prevail in generating most of the cloud ice (about 99%).

Figure 5c shows that homogeneous freezing is the largest contributor (~93% of the total budget) because, at temperatures below −36°C, all the cloud droplets freeze to form cloud ice. The cloud ice formed by all the SIP processes contributes up to 6% of the total budget. Heterogeneous ice nucleation contributes only about 1% to the total budget. Figure 5d shows the breakup in ice–ice collisions is the largest contributor for the cloud-ice mass mixing ratio.

In Fig. 5b, in the mixed-phase region, major contributions to overall particle number concentrations come from cloud ice and snow with a small contribution from graupel/hail.

Figure 5e shows the budget of the total number concentration of ice particles initiated throughout the simulation from various sources. Cloud ice generates about 98% of all ice particles, whereas snow and graupel/hail contribute about 1.5% and 0.2%, respectively. Despite its low number of particles, graupel/hail is important for the mass of condensate aloft and enables treatments of fragmentation processes and riming, as well as realistic precipitation production.

New parameterization can predict the detrainment in the convection plume due to the addition of its dependency on buoyancy and turbulence. The detrainment rate predicted by the ZM scheme is only at one height level at 9 km because the detrainment rate was evaluated only for levels above the level of the maximum entrainment rate (appendix D, Fig. D1).

5. Results from sensitivity simulations

Sensitivity simulations were performed by comparing perturbation simulations described in Table 3 with the ACC_24 run (section 4.4). The simulations assess the roles of CCN and solid aerosols, the time dependence of INP activity, and the occurrence of the SIP processes in the MC3E storm (section 3b and section 4.4). The simulations are done by prohibiting the target process or by altering some environmental factor relative to the ACC_24 simulation, so as to reveal its role. The representation of each perturbation simulation is identical to the ACC_24 run in all other respects.

a. Comparison between the SZ11 scheme and the ACC scheme

To reveal the importance of the new parameterization, the ACC_24 run was compared with the original unmodified implementation by SZ11 of convection in the ZM scheme.

In Fig. 6a, the averaged CDNC at cloud base for the ACC_24 is about 1080 cm^{-3} and SZ11 predicts 25 cm^{-3}, which is 1.5 orders of magnitude too low compared to observations (section 4). Figure 6b shows the LWC predicted by the ACC_24 reaches a maximum of 2.4 g m^{-3} at −4°C, almost twice that of the SZ11 run which is 1.1 g m^{-3}. The SZ11 predicts cloud liquid above the homogeneous freezing level (about −36°C).

Figure 6c shows the ACC_24 case has a maximum vertical velocity of 15 m s^{-1}, which is typical for deep convection. SZ11 attains a maximum vertical velocity of only 5 m s^{-1}. The difference in the vertical profile of vertical velocity between the ACC_24 and SZ11 cases is because of vertical velocity sensitivity to different microphysical treatments of convective ice and liquid water through altered latent heat and gravitational burden of condensate. An unrealistic deceleration of the updraft speed is predicted at levels from 12° to 5°C, in the SZ11 case. To prevent such decelerations in the ACC

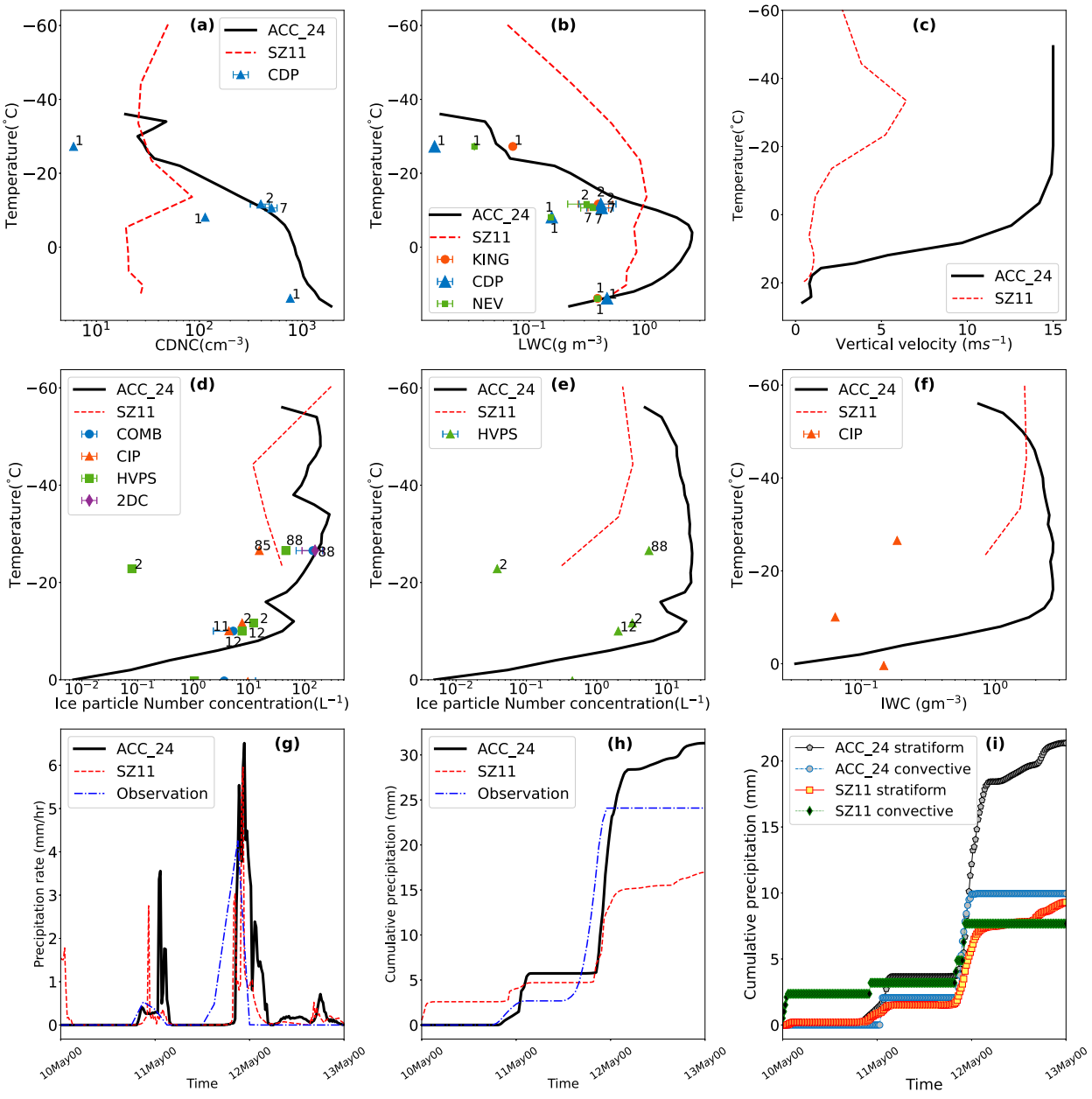

FIG. 6. Predicted (a) cloud droplet number concentration compared with observations from the CDP probe; (b) LWC compared with CDP, KING, and Nevzorov probes; (c) vertical velocity profile; (d) total concentration of ice particles with sizes > 0.2 mm compared with observations from the 2DC, CIP, HVPS-3 probe, and COMB; (e) total ice number concentrations of all ice particles with size > 1 mm compared with aircraft observations from the HVPS-3 probe; and (f) total IWC from the SZ11 (solid red line with square) and ACC (solid black line with pentagram) simulations. The cloud microphysical properties are conditionally averaged over cloudy convective updrafts ($w_{up} > 3$ m s^{-1}). Predicted (g) precipitation rate (mm h^{-1}) and (h) cumulative surface precipitation from the SZ11 (dashed red line) and ACC_24 (solid black line) simulations compared with observations (Xie et al. 2014). Predicted (i) stratiform and convective cumulative precipitation from the SZ11 and ACC_24 simulations.

simulations, modification to the ECMWF formula of vertical velocity was done, as described above [section 2d(3)].

Figure 6d shows that SZ11 shows a good agreement with the observations for the level −25°C. However, below −25°C, SZ11 underpredicts the number concentration of ice particles.

Figures 6d–f show that SZ11 does not predict ice particles below the −15°C level. The ACC scheme is better at predicting the ice concentration (Fig. 4) than the SZ11 in view of the validation noted above. The SZ11 scheme has erroneous predictions generally.

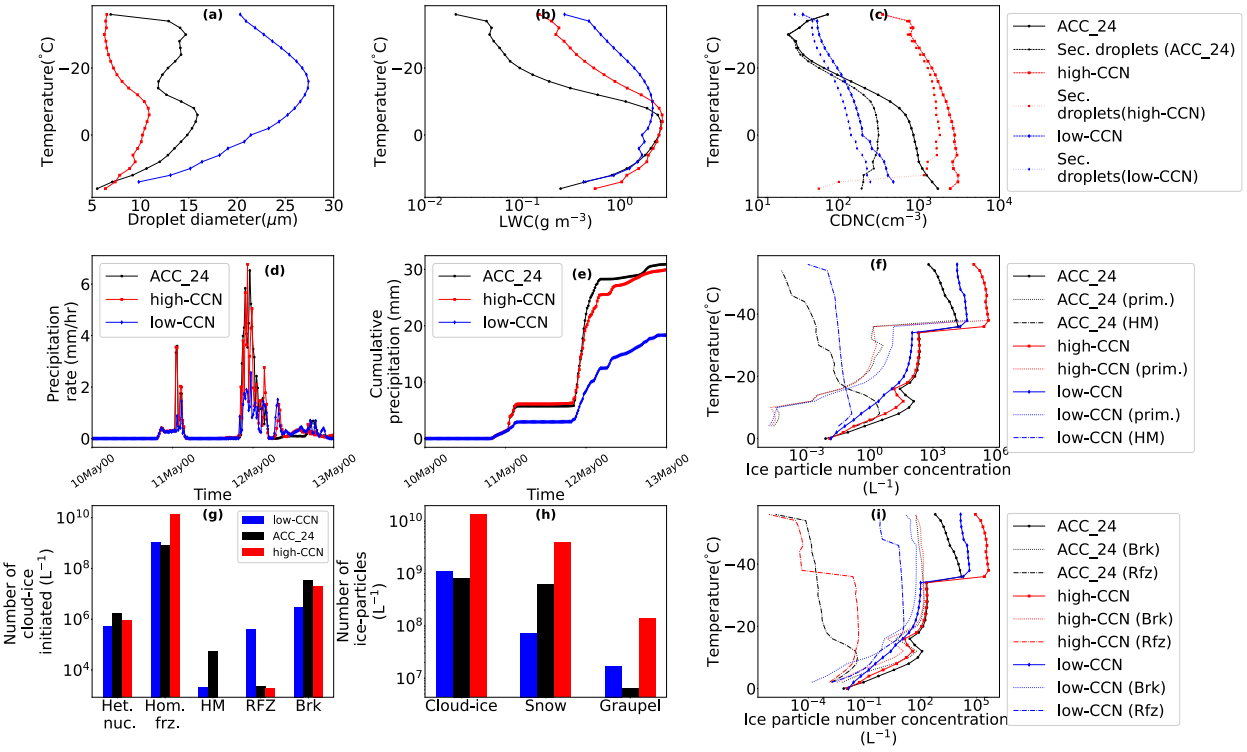

FIG. 7. (a) Predicted mean cloud droplet diameter, (b) predicted LWC and (c) predicted CDNC plotted with secondary droplets, (d) surface precipitation rate (mm h^{-1}), (e) cumulative surface precipitation (mm), and (f) total ice particle number concentration with tagging tracers from cloud ice from primary ice processes ("prim.") (dotted line), HM process (dash dotted line), and (i) total ice particle number concentration with tagging tracers from breakup in ice–ice collisions ("Brk") (dotted line), raindrop freezing fragmentation process (Rfz) (dash dotted line) from the high-CCN (solid red line with squares), low-CCN (solid blue line with diamond), and ACC_24 (solid black line with pentagram) simulations. The cloud microphysical properties are conditionally averaged over cloudy convective updrafts ($w_{up} > 3$ m s^{-1}). Bar plot for the (g) budgets of the number of cloud-ice particles initiated from heterogeneous ice nucleation (Het. nuc.), homogeneous freezing (Hom. frz.), breakup in ice–ice collisions (Brk), raindrop freezing fragmentation (Rfz), and HM process and (h) budgets of the number of cloud ice, snow, and graupel particles initiated in the cloud for the ACC_24 (black colored bars), high-CCN (red colored bars), and low-CCN (blue colored bars) simulations.

Nevertheless, the SZ11 parameterization is able to predict the two peaks as shown in Fig. 6f. SZ11 underestimates the peak rates of precipitation, the first peak being 56% of the observation and the second peak being 79% of the observed value. The cumulative precipitation at the end of the simulation (Fig. 6g) is 30% too low for the SZ11 scheme which is much less accurate than the ACC_24 (only 8% too high). ACC is able to predict the first peak, but the intensity is higher than the observations.

The addition of the new detrainment scheme [section 2d(2)] results in an increase in the stratiform precipitation, as seen in Fig. 6i. This increase is due to stronger, more realistic outflow from convection to the stratiform cloud shield.

b. *Time dependence of heterogeneous ice nucleation*

A simulation was conducted to study the impact on the convective microphysics from the inclusion of time dependence of INP activity. The time dependence of INP activity described above [section 2e(2)] is implemented in the EP, and the results are compared with the ACC_24 case.

Figures D2a–c reveal that the properties of cloud droplets do not show significant variation when the time dependence is included. Figure D2d shows that the total number concentrations of ice particles are not influenced by the time dependence. The heterogeneous ice component of the ice concentration from the tagging tracer (Fig. D2e) is altered by less than 0.4 L^{-1} (<0.5% change) when time dependence is included. In short, this reveals only a limited effect from including time dependence of INP activity for the predicted properties of the deep convection core, with ice multiplication amplifying the effect of primary ice with repercussions on supercooled liquid and homogeneous freezing later in the ascent. Figure D2f shows no difference in the cumulative precipitation between time dependence and ACC_24 simulation.

c. *Solute aerosols in the environment*

To study how the ACC scheme represents the influence from CCN on the convective clouds, changes to the environmental concentrations of soluble aerosols were done as described in Table 3. This involves a height-dependent factor

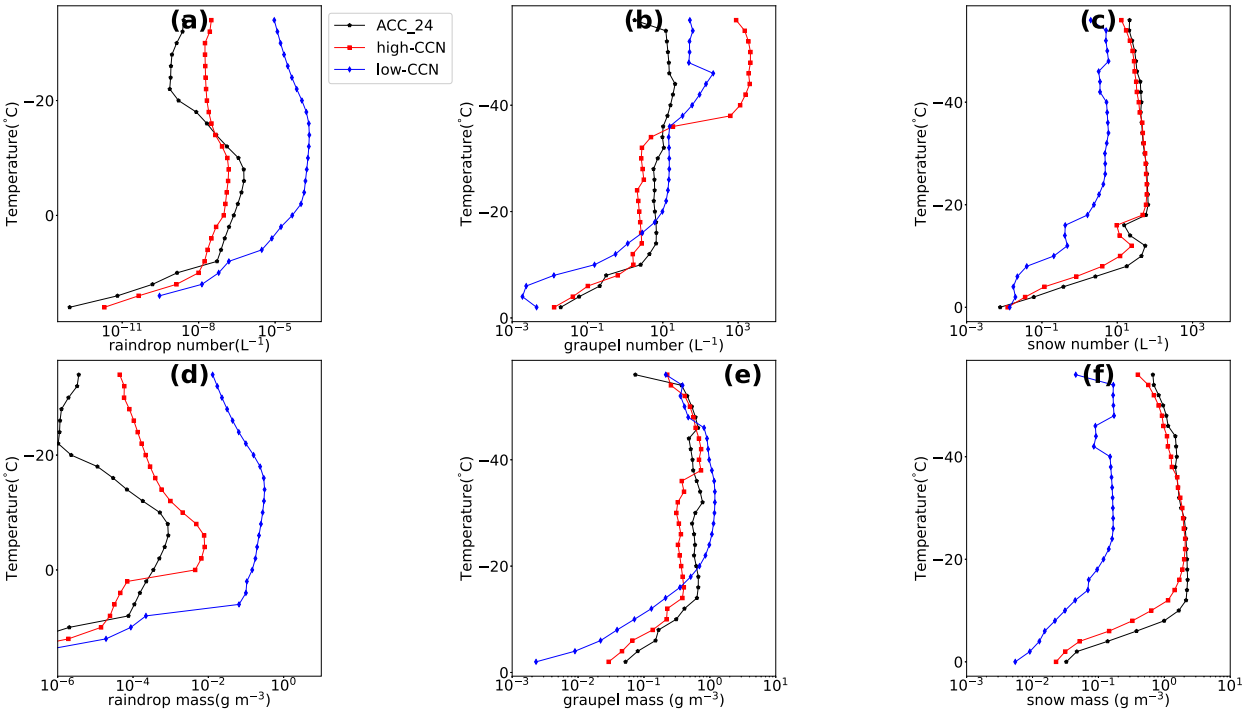

FIG. 8. Predicted (a) rain number concentration, (b) graupel number concentration, (c) snow number concentration, (d) rain mass mixing ratio, (e) graupel mass mixing ratio, and (f) snow mass mixing ratio, from the high-CCN (solid red line with squares), low-CCN (solid blue line with diamond), and ACC_24 (solid black line with pentagram) simulations. The cloud microphysical properties are conditionally averaged over cloudy convective updrafts ($w_{up} > 3$ m s^{-1}).

applied to the aerosol loading in the ACC_24 simulation to represent the polluted continental-versus-maritime contrasts. The parameterizations described above [sections 2e(1)(i) and 2e(1)(ii)] treat the CCN activation to form cloud droplets in the bulk plume.

Figure 7a shows that stronger condensational growth of droplets in the low-CCN case results in the mean droplet diameter reaching a maximum of 24 μm at about the −18°C level. Such large diameters of cloud droplets would be expected to boost coalescence aloft to form rain. In the mixed-phase region, the raindrop freezing fragmentation and HM processes are predicted to produce significant splinters/fragments of ice, which is confirmed in the budget of ice initiation in Fig. 7g.

Figure 7b reveals that below the freezing level, LWC is increased by up to a factor of 6 in the high-CCN case relative to the ACC_24 due to reduced collision–coalescence from smaller cloud droplets with lower collision efficiencies. The LWC is unchanged for the low-CCN case relative to the ACC_24 at those levels. There is a qualitatively similar trend at subzero aloft except that above the −15°C level, the low-CCN case has a higher LWC (Fig. 7b) than the ACC_24 because of less riming of cloud liquid by much less snow (Fig. 8d).

At the cloud base in Fig. 7c, the concentration of cloud droplets is increased and decreased by about a factor of 3 relative to ACC_24 for the high-CCN and low-CCN cases, respectively. In the low-CCN case, since a higher proportion of CCN is activated near cloud base, there is a less relative contribution from in-cloud activation aloft than in the ACC_24 and high-CCN cases. In the high-CCN case, the increased number of cloud droplets results in reduced coalescence due to their smaller size causing the higher LWC below the freezing level relative to the ACC_24 (Fig. 7a).

Figures 8a and 8d show an increase in the predicted raindrop mass and number by a factor of 100 relative to ACC_24 for the low-CCN case. The high-CCN case shows a decrease in the predicted raindrop mass and number by a factor of 3. This increase in the raindrop mass is due to the collision–coalescence of the large cloud droplets.

Figures 7f and 7g show that in the mixed-phase region, the number concentration of ice particles increases and decreases by a factor of up to 2 in the high-CCN and low-CCN cases, respectively, relative to ACC_24. In the high-CCN case, below −16°C, the number particle concentration is less than the ACC_24 by a factor of 3, and this decrease is caused by a less intense breakup in ice–ice collisions. Similarly, in the low-CCN case, a reduction in the activity of the breakup in ice–ice collisions leads to a decrease in ice particle concentration by about 30% compared to the ACC_24. The simulated trend of increasing ice concentrations in the mixed-phase regions with increasing CCN is due to the intensification of the breakup in graupel–snow collisions, which in turn is inexplicable in terms of decreasing coalescence with smaller cloud droplets causing less warm rain and less accretion of cloud liquid during the ascent up to the interior of the mixed-phase region, as the CCN loading increases, which boosts the supercooled liquid which is the source of graupel mass by riming in the simulation.

Above the mixed-phase region, the effect of the homogeneous freezing of cloud droplets to form cloud ice can be seen. Figure 7g also shows that the cloud ice formed by homogeneous freezing is approximately doubled for the low-CCN cases and increased by an order of magnitude for the high-CCN cases relative to the ACC_24 due to the similarly complex response of supercooled cloud droplet number near the −36°C level, as noted above. A similar increase is also seen in the budget for cloud ice in Fig. 7h. The homogeneous freezing process dominates the budget of cloud-ice particles by about two orders of magnitude relative to secondary ice in all three cases.

Figure 7h shows an increase in snow initiated by a factor of 6 and a decrease by a factor of 10 for the high-CCN and low-CCN cases, respectively. Also, it shows an increase in graupel initiated by a factor of 20 and 3 for the high-CCN and low-CCN cases, respectively. Figures 8c and 8f show a decrease in the snow number up to a factor of 20 relative to ACC_24 and a decrease in the snow mass up to 20% for the low-CCN case. For the low-CCN case, riming of LWC is driving the sensitivity below −35°C. Below −20°C, snow is depleted by producing a graupel-by-graupel autoconversion process. Above −35°, large supercooled cloud droplets homogeneously freeze to form cloud ice. This cloud ice interacts with graupel to produce smaller graupel fragments, thus driving up the graupel number concentration.

Figures 7d and 7e show only a slight decrease of 3% in the cumulative surface precipitation from the ACC_24 run to the high-CCN case. However, in the low-CCN case, larger cloud droplets strengthen the depletion of snow by accretion onto graupel relative to the ACC_24. This in turn weakens the accumulated surface precipitation by about 15% compared to the ACC_24, which is mostly due to the response of the convective precipitation.

d. Solid aerosols in the environment

Heterogeneous ice nucleation by INPs initiates primary ice which later grows to become precipitation that produces secondary ice in clouds. The response of the convective microphysics to changes in the environmental concentration of insoluble aerosols (INPs) is evaluated. These concentrations were changed by a height-dependent factor up to 10 throughout the mid- and lower troposphere with the greatest change being near the ground (Table 3). This factor accounts for the continental-versus-marine contrasts seen in aerosol conditions in the background troposphere. In ACC, the solid aerosol particles initiate cloud droplets and cloud ice from their CCN and INP activity, respectively. INPs can be interstitial aerosols, and this is treated in the in-cloud droplet scheme [section 2e(1)(ii)]. The interstitial aerosols can then activate to produce cloud droplet [section 2e(1)(ii)].

Figure 9a shows a trend of decreasing mean droplet diameter with increasing solid aerosol loading with a maximum of 12 μm aloft in the high-INP case. For the low-INP case, the mean droplet diameter does not show significant change, and it increases by only about 0.5 μm compared to ACC_24. For the high-INP case, more numerous cloud droplets initiated lead to a decrease in the collection efficiency of the cloud droplets resulting in smaller droplet diameter and reduced formation of rain.

Figure 9b shows that the LWC of the low-INP case closely follows the ACC_24. In the high-INP case, the same applies below the −10°C level, but above this level, the LWC is increased up to 60% relative to ACC_24. This increase in LWC is because of a reduced riming with snow and graupel.

In Fig. 9c, at cloud base, the CDNC for the high-INP case is changed by a factor of 2 relative to the ACC_24, and for the low-INP case, it is decreased by 30%. The CDNC profiles for the low-INP case closely follow the ACC_24. The secondary droplets initiated by the coated solid aerosols are increased by an order of magnitude for the high-INP case and decreased up to a factor of 4 for the low-INP case relative to the ACC_24.

Figure 9f shows that in the mixed-phase region of 0° to −35°C the total ice particle concentration is dominated by the breakup in the ice–ice collisions in both the low- and high-INP cases as in the ACC_24. Consequently, the total ice concentration in both the low-INP and high-INP cases is similar to the ACC_24 with only a minor boost by a factor of 2 from the ACC_24 case to the high-INP case.

Figure 9g shows the budget for cloud ice initiated by heterogeneous nucleation for the high-INP case is increased by a factor of 3 relative to ACC_24 and is reduced by a factor of 6 for the low-INP case. The number of ice fragments from breakup in ice–ice collisions is relatively insensitive to the changes in INP, with only a change by a factor of 2 from the low-INP case to the high-INP case, exceeding the cloud ice initiated from heterogeneous nucleation by up to about an order of magnitude.

Figure 9g also shows a reduction in the budget of the cloud ice initiated by raindrop freezing fragmentation and the HM process for the high-INP case relative to the ACC_24. These processes are weak in the MC3E storm simulated here, due to the small mean size of the droplets (<12 μm), which decreases from the low-INP case to the high-INP case inhibiting both SIP processes. The number of cloud ice formed by homogeneous freezing is increased by a factor of 2 compared to the low-INP case.

In Fig. 9h, an increase in the budget of cloud ice initiated by 25% relative to ACC_24 is seen in the low-INP case. The budget for cloud ice is increased by a factor of 1.5 relative to ACC_24 for the high-INP case. From the low-INP case to the high-INP case, there is an increase in the snow and graupel initiated by 60%. In Fig. 9d, the precipitation rate at the second peak is increased by 2 mm h^{-1} from ACC_24 for the high-INP case, whereas the low-INP case is the same as ACC_24. In Fig. 9e, cumulative surface precipitation at the end of the simulation shows no change for both the high- and low-INP cases.

e. Processes of secondary ice production

Various measurement and modeling studies have shown that SIP mechanisms are prolific (Mace et al. 2009; Field et al. 2017; Huang et al. 2017; O'Shea et al. 2021; Atlas et al. 2022). Field et al. (2017) underlined three SIP mechanisms, and the influence of these SIP mechanisms has been investigated in the following sensitivity analysis. SIP mechanisms have been

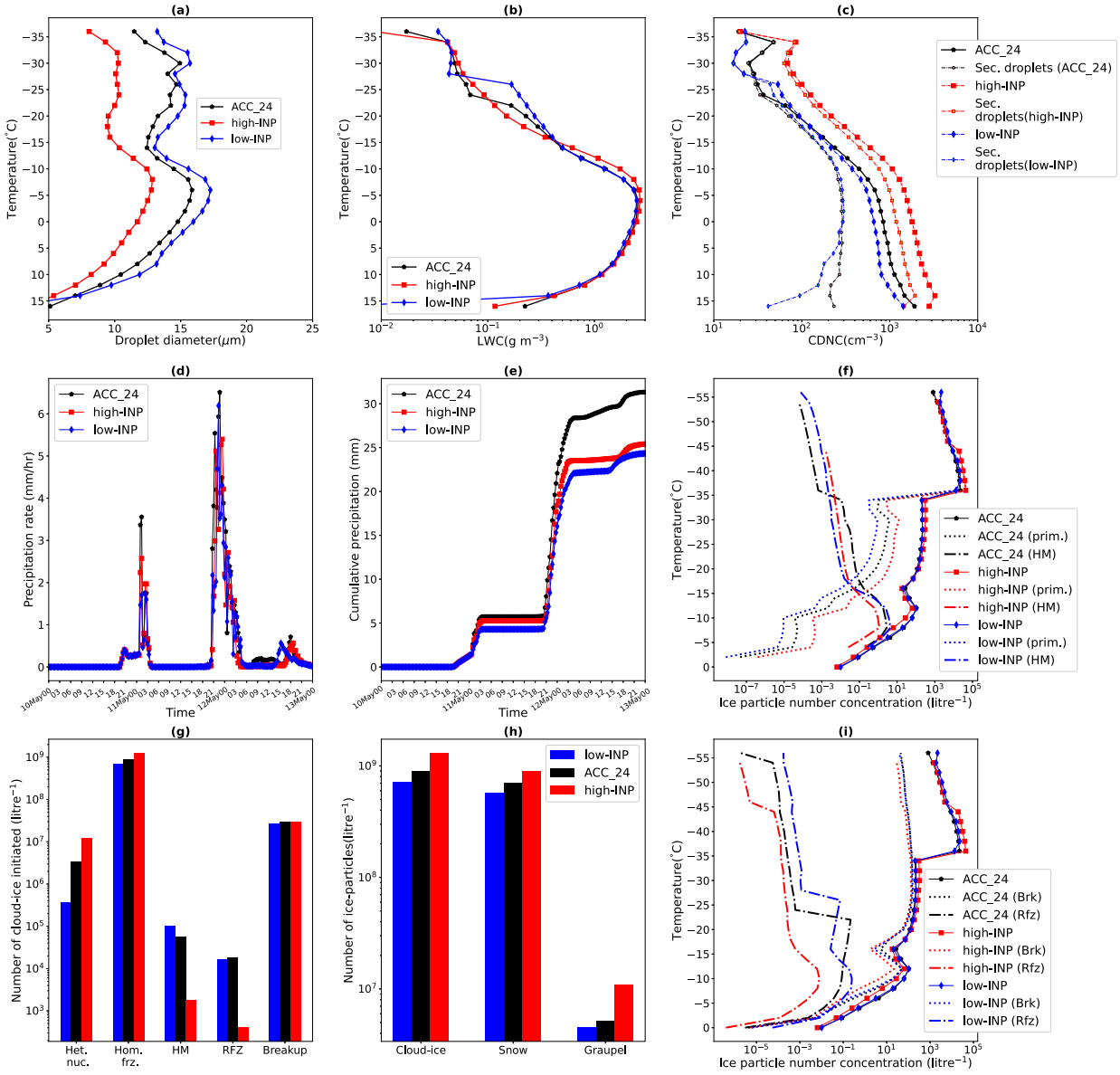

FIG. 9. (a) Predicted mean cloud droplet diameter, (b) predicted LWC and (c) predicted CDNC plotted with secondary droplets, (d) surface precipitation rate (mm h^{-1}), (e) cumulative surface precipitation (mm), and (f) total ice particle number concentration with tagging tracers from cloud ice from primary ice processes ("prim.") (dotted line), HM process (dash dotted line), and (i) total ice particle number concentration with tagging tracers from breakup in ice–ice collisions (Brk) (dotted line), raindrop freezing fragmentation process (Rfz) (dash dotted line) from the high-INP (solid red line with squares), low-INP (solid blue line with diamond), and ACC_24 (solid black line with pentagram) simulations. The cloud microphysical properties are conditionally averaged over cloudy convective updrafts ($w_{up} > 3$ m s^{-1}). Bar plot for the (g) budgets of the number of cloud-ice particles initiated from heterogeneous ice nucleation (Het. nuc.), homogeneous freezing (Hom. frz.), breakup in ice–ice collisions (Brk), raindrop freezing fragmentation (Rfz), and HM process and (h) budgets of the number of cloud ice, snow, and graupel particles initiated in the cloud for the ACC_24 (black colored bars), high-INP (red colored bars), and low-INP (blue colored bars) simulations.

switched off alternatively, and another case with all the SIP mechanisms switched off has been simulated.

The no-raindrop-freezing-fragmentation and no-HM cases closely follow the profiles of the ACC_24 simulation for the cloud liquid and ice particle properties (Figs. 10 and 11). Also, Fig. 5c shows that the contribution from the HM process and raindrop freezing fragmentation is less compared with other processes. So, switching off these two processes has a negligible effect on the simulation.

In the no-ice–ice collisional breakup simulation, the cloud droplet diameter is increased by 2–3 μm in the mixed-phase region. CDNC and LWC are increased by a factor of 2–3 in the region above the −20°C level. In the mixed-phase region, total ice particle concentration in the no-ice–ice collisional breakup

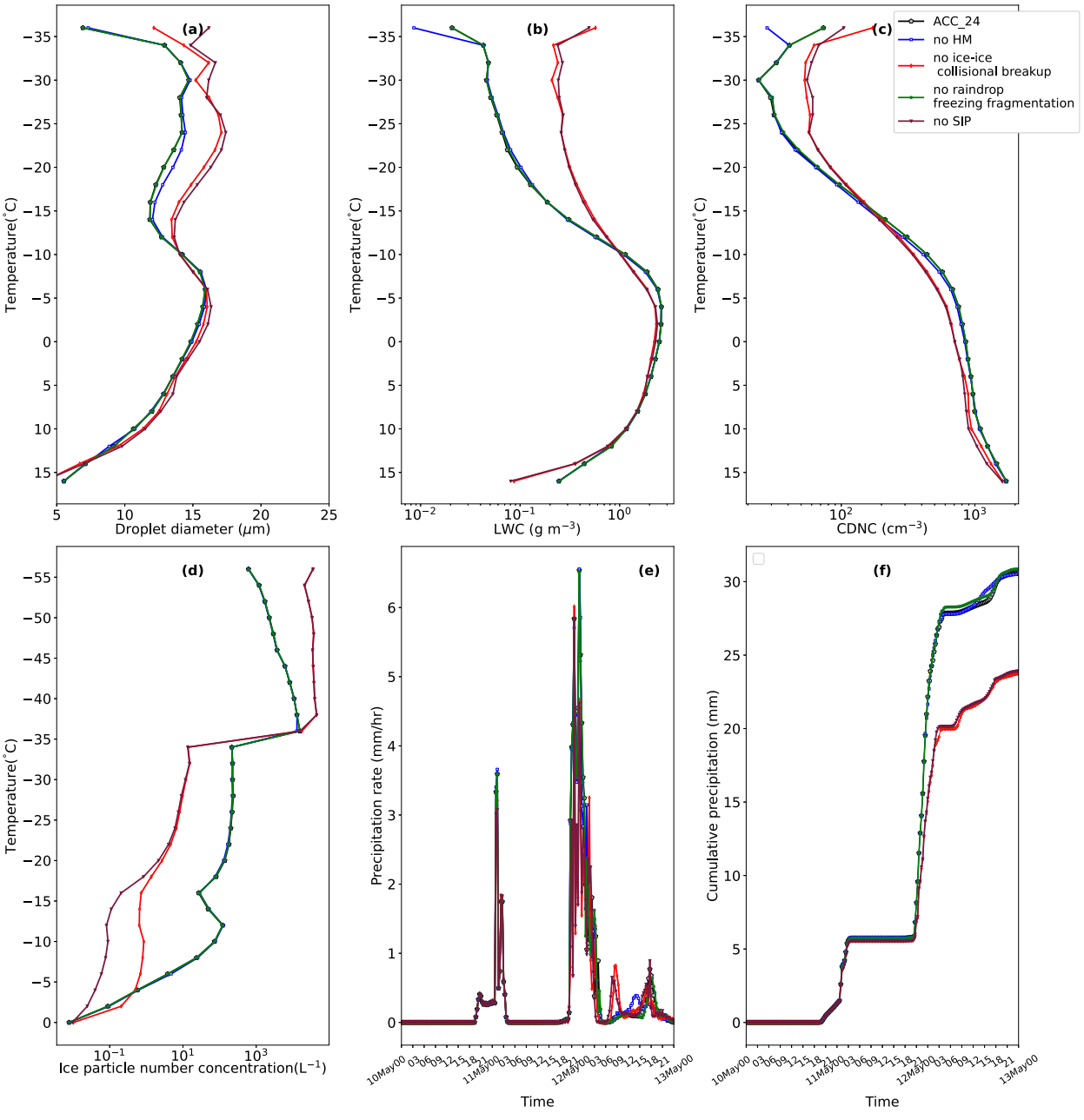

FIG. 10. (a) Predicted mean cloud droplet diameter, (b) predicted LWC and (c) predicted CDNC plotted with secondary droplets, (d) total ice particle number concentration, (e) surface precipitation rate, and (f) cumulative surface precipitation from the no-HM (solid blue line with squares), no-ice–ice collisional breakup (solid line with red square), no-raindrop-freezing-fragmentation (solid green line with circle), no-SIP (solid purple line with inverted triangle), and ACC_24 (solid black line with pentagram) simulations. The cloud microphysical properties are conditionally averaged over cloudy convective updrafts ($w_{up} > 3$ m s^{-1}).

simulation (Fig. 10d) reduces by a factor of 10–200 compared to the ACC_24. Figure 11b shows a significant decrease in the snow and graupel/hail for the no-ice–ice collisional breakup run. The reduced cloud-ice number concentration leads to decreased activity of aggregation of cloud ice to form snow and also less snow accreting on cloud ice. SIP mechanisms include the interaction of ice crystals with the supercooled liquid in the clouds to form fragments, and this acts as a sink for cloud liquid. The decrease in ice particles leads to less depletion of cloud liquid by riming, thus increasing LWC, CDNC, and droplet diameter above −10°C. Figure 11 shows the budget for graupel initiated in the simulation is reduced by about two orders of magnitude compared to ACC_24. Similarly, the budget of cloud ice and snow initiated is reduced by an order of magnitude relative to ACC_24. The cumulative precipitation is reduced by 6 mm because of a decrease in ice precipitation.

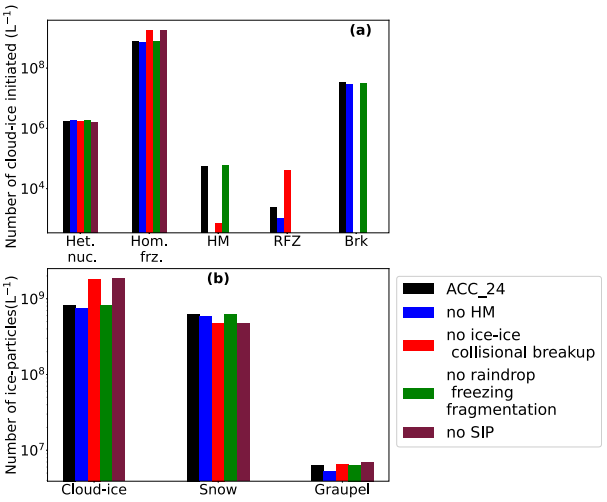

FIG. 11. Bar plot (a) for the budgets of the number of cloud ice from heterogeneous ice nucleation (Het. nuc.), homogeneous freezing (Hom. frz), breakup in ice–ice collisions (Brk), raindrop freezing fragmentation (Rfz), and HM process and (b) budgets of the number of ice particles from cloud ice, snow, and graupel number concentration in the cloud for the ACC_24, no-HM, no-ice–ice collisional breakup run, no-raindrop-freezing-fragmentation, and no-SIP simulations.

For the no-SIP case, it follows the same trend as the no-ice–ice collisional breakup case for all cloud properties. The ice particle number concentration is reduced more in the no-SIP case than in the no-ice–ice collisional breakup in the regions −5° to −10°C. This is because of the inactive HM process in the no-SIP case.

f. Coalescence

An additional sensitivity simulation was done, where the coalescence of cloud droplets was switched off, both in the stratiform microphysics and in the ACC scheme. This simulation was compared with the ACC_24 run. The results show a decrease in cumulative surface precipitation by 12%, indicating the ice crystal processes contribute up to 88% to the cumulative surface precipitation (appendix D, Fig. D3). The corresponding reduction in the convective surface precipitation is 20%. This agrees well with the high-resolution cloud modeling by Gupta et al. (2023) who found that 80% of the total surface precipitation was from the ice crystal processes in their simulations of the MCS event of the MC3E campaign.

6. Summary

The convection parameterization of the CESM global model has been improved for more realism of cloud dynamics and microphysics in an aerosol-sensitive manner with the new ACC scheme. Specifically, this has been done by including the hybrid bin/bulk microphysical routines from the high-resolution AC model (section 2a).

The parcel approach of the ACC scheme is able to resolve the cloud processes at fine vertical resolution and follows the microphysical evolution of hydrometeors. The latest treatments of three SIP processes, namely, HM process/rime splintering, raindrop freezing fragmentation, and breakup in ice–ice collisions for all permutations of colliding microphysical species, are included based on recent results from cloud modeling (Waman et al. 2022). A novel feature is the inclusion of graupel/hail as a microphysical species in contrast with the original version of the convection scheme.

Validation of the ACC scheme is performed with aircraft and ground-based observations from the MC3E campaign. The adequate agreement between observed and predicted quantities is consistent with the realism of the representations of initiation of cloud droplets and cloud ice and of growth processes such as collisional coagulation. In particular, the realism of simulated cloud droplet concentrations near cloud base suggests that the aerosol activation and aerosol–cloud interaction for the liquid phase are represented accurately. Aloft in the convective plume, the average LWC lies near the middle of the observed range of 0.02–2.6 g m^{-3}. Such convective cloud properties are representative of the globe. For example, LWC in convective clouds over Oklahoma with high vertical velocities can be up to 5 g m^{-3} or more (Poellot and Pflaum 1989). Prabha et al. (2011) over India observed that convective clouds during premonsoon and monsoon conditions have an LWC in the range of 0.5–2 g m^{-3}, and Rosenfeld and Woodley (2000) showed that deep convective clouds have an LWC up to about 1.8 g m^{-3}.

Cloud models historically have generally shown a tendency to underpredict the ice concentration (e.g., Fridlind et al. 2007; Lasher-Trapp et al. 2016; DeMott et al. 2016; Field et al. 2017). In the ACC scheme, we obtain an accurate prediction of the ice crystal concentration that is in the range of the aircraft observations. The inclusion of graupel/hail in the ACC scheme as an additional microphysical species has enabled detailed treatment of microphysical processes such as SIP mechanisms and autoconversion of graupel/hail. In section 4, the predicted snow and graupel mass contributes up to 96% of the total ice mass. This high mass of snow and graupel would have a fast mass-weighted fall speed and impact the precipitation timing. The accumulated surface precipitation has an error of only 20% at the end of the simulation. This gives us confidence in simulating aerosol–convection interactions with the ACC scheme.

Various sensitivity simulations were performed. These demonstrate that the simplified dynamical treatment of convection in a typical parameterization of a global model can represent some of the microphysically complex responses to changes in environmental conditions:

- The increased number concentrations of cloud droplets for the high-CCN case increase the cumulative surface precipitation by only about 1 mm relative to the ACC_24. The response of LWC reverses at the −15°C level. Homogeneous freezing of cloud droplets near −36°C produces the vast majority of all cloud-ice particles in all simulations, generally increasing with CCN aerosol loadings.
- For the high-INP case, increasing the loadings of solid aerosol particles results in an increase in concentrations of cloud droplets and of cloud ice both from heterogeneous ice nucleation

and from homogeneous freezing relative to the ACC_24. A corresponding increase in the activity of breakup in the ice–ice collisions increases the number concentration of ice particles by a factor of 2 in the mixed-phase region.

- Switching off various SIP processes shows breakup in ice–ice collisions is the most prolific in the mixed-phase region:
  - Without a breakup in ice–ice collisions, it is not possible to get any validation in the ice concentrations in the convective plume, as found in other recent studies (Waman et al. 2022, 2023).
  - Raindrop freezing fragmentation had the least effect among all the SIP processes in the sensitivity simulations.
- Breakup in ice–ice collisions acts as a buffer reducing the sensitivity to the environmental aerosol conditions.

The aerosol sensitivity studies (high CCN, low CCN, high INP, and low INP) illustrate a complex response of the simulated deep convective system to environmental aerosol loading. The changes in aerosol loading affect the sources and sinks of microphysical species through the many feedback processes, such as the efficiency of accretion of droplets by collision–coalescence which affects the number and mass of the cloud droplets and in-cloud activation through the supersaturation. Another feedback process is the gravitational burden of the condensate in the parcel, which affects the effective buoyancy and convective ascent (Patade et al. 2022).

Generally, in warm-based clouds, the warm part of the cloud may determine the properties of the cloud droplets and raindrops reaching the freezing level if warm rain can occur there (Phillips 2024), thus affecting the ice processes in the subsequent ascent above it from freezing of cloud liquid and raindrops. However, the MC3E simulated here involves a cloud base that is not so warm with the continental aerosol conditions, so little rain forms.

Our findings reveal that cloud droplet properties in the convective plume are sensitive to perturbations in environmental aerosol concentrations regarding both soluble and solid aerosol materials (CCN and INPs). A general trend of the number concentration of cloud droplets increasing with the aerosol loadings is seen at all levels. Although as expected, there is more sensitivity to the soluble aerosol loading than for solid aerosols; nevertheless, it is intriguing that there is a significant sensitivity of the cloud droplet number to the solid aerosols by a factor of 2 from the low- to high-INP cases (Twohy et al. 2009). Correspondingly, more numerous cloud droplets cause more cloud-ice particles to be initiated by homogeneous freezing in the anvil of the deep convective cloud, for example, from the low-CCN to high-CCN cases or from the ACC_24 to high-INP cases. For the low-CCN case, the mass of ice particles decreased by up to 60% relative to the ACC_24, which is similar to sensitivity studies performed by Gupta et al. (2023). Gupta et al. (2023) predicted a decrease by up to 75% for a simulation similar to the low-CCN case relative to ACC_24, with the high-resolution AC model. In the mixed-phase region of the deep convective bulk plume simulated with the ACC scheme, breakup in ice–ice collision mechanism is predicted to be the most prolific mechanism by far and acts to enhance ice concentrations by up to an order of magnitude compared to the cloud ice initiated by heterogeneous ice nucleation. This is why SIP acts to reduce the simulated sensitivity of the cloud glaciation with respect to soluble and solid aerosol conditions in the environment, as noted above.

Simulations conducted to study the role of SIP mechanisms showed that when breakup in ice–ice collisions is switched off, the LWC was doubled or tripled in the mixed-phase region above the −12°C level. Similar changes in LWC were observed when all SIP mechanisms were switched off, indicating a dominant effect from a breakup in ice–ice collisions in the simulated convective plume. By contrast, prohibiting raindrop freezing fragmentation did not significantly affect the cloud droplet properties or ice concentrations in the simulations. Also, switching off the HM process resulted in an increase in LWC and CDNC by only about 15% in the mixed-phase region.

Moreover, regarding impacts on the cloud glaciation, the total ice concentration was most affected when all the SIP mechanisms were switched off and also when breakup in ice–ice collisions was prohibited. In the ACC_24 simulation of MC3E, breakup in ice–ice collisions prevails in the overall ice multiplication and ice concentrations are reduced by a factor of 20–200 in the mixed-phase region when it is switched off. In and above the mixed-phase region of the convective plume, breakup in ice–ice collisions and homogeneous freezing are the leading sources of cloud ice, respectively.

Including time dependence of heterogeneous ice nucleation in the EP has a negligible impact on the simulated primary cloud ice formed by heterogeneous ice nucleation (tagging tracer) and even less impact on the total ice concentrations. Also, in the mixed-phase region, the leading SIP mechanism (breakup in ice–ice collisions) initiates about 80% of the total cloud ice, while heterogeneously nucleated ice contributes up to 20% (including levels above the mixed-phase region) according to the predicted budget. Tagging tracers show that in the mixed-phase region the ice concentrations are enhanced by about two orders of magnitude relative to the primary ice. Consequently, for the MC3E convection case, the overall effect of this time dependence is predicted to be negligible.

The empirical basis for our representation of this time dependence is the laboratory observations of real aerosol samples by Jakobsson et al. (2022). They observed that at time scales of a few minutes, there was only a small shift in the average freezing temperature of INPs (after 3 min of constant isothermal conditions, this temperature was warmed by 0.3 K) and therefore a weak time dependence. The laboratory observations by Jakobsson et al. (2022) are robust and representative of the troposphere because many contrasting airmass types were sampled in southern Sweden at various times of the year and were dominated by a wide range of aerosol conditions. The sampled solid aerosol material was studied in isothermal laboratory experiments for long times of up to about 10 h.

In the present simulation of the MC3E storm, there is a fast vertical velocity in the bulk plume during convective episodes and the time scale of parcel ascent through the mixed-phase region is typically about 5 min. Such fast convective ascent would be expected to show a weak time dependence, as is

indeed predicted here. Waman et al. (2023) simulated various campaigns and showed that the effect of time dependence is diminished (<10%) for clouds with a short lifetime (<90 min) and intense vertical motions. They noticed an increase in the predicted total ice concentration by a factor of about 2 at levels colder than −15°C.

Even though the ACC scheme is able to represent the complex behavior of the detailed microphysical conversions among hydrometeors in deep convection as a function of environmental conditions, our results have some limitations. First, the simplified 1D structure of the initial observed state of the atmosphere with which to drive the simulation, and the artificially 1D representation of deep convection with a single bulk plume, causes a lack of accuracy in treating the fine-scale cloud structures. For instance, the downwelling of homogeneously nucleated ice into the mixed-phase region for recirculation into the convective updraft is missed (Heymsfield et al. 2005). Second, for the same MC3E storm, the ACC scheme shows more sensitivity to CCN aerosol conditions than the 3D high-resolution cloud simulation by Gupta et al. (2023), for both precipitation and cloud microphysical properties. For instance, the ACC scheme predicted a 20% decrease in cumulative surface precipitation (mostly cold) from the ACC_24 to low-CCN cases, whereas Gupta et al. (2023) predicted a corresponding decrease in cumulative cold surface precipitation by about 5%, which was overwhelmed by a larger increase in the warm surface precipitation.

In reality, it is a challenge to reproduce the same sensitivity as in the 3D cloud model because cold and warm types of precipitation have opposite sensitivities with respect to aerosol conditions (Gupta et al. 2023) and are finely balanced. This limitation is an inevitable classic symptom of the simplistic dynamics of convection, which in reality is dynamically forced by fine-scale processes, such as overturning and density currents in the PBL triggering new cells, which artificially inhibit coalescence by omitting in-cloud mixing and spatial variability of aerosol conditions. Finally, the ACC scheme incurs extra computational expense compared to the original SZ11 scheme, with the refined representation of the subgrid-scale microphysical processes causing runs to take 3 or 4 times longer to complete.

Another issue is that the present simulations include graupel/hail and corresponding SIP mechanisms only in the deep convective microphysics. The large-scale cloud scheme with stratiform microphysics given by Morrison and Gettelman (2008) in public CAM6 does not yet include graupel/hail. Soon, a viable version of CESM treating graupel/hail in the large-scale cloud scheme will become available (Gettelman et al. 2019a).

Here, simulations have been conducted for a single column and detailed deep convective microphysics. The current scheme provides a framework for a unified microphysical representation for the large-scale and convective clouds in the global model. Future developments of CESM can be easily assimilated into this framework.

In conclusion, the implementation of the ACC scheme for convective clouds provides adequate realism in the representation of aerosol–cloud interactions and cloud microphysical processes. The various sensitivity studies show that the model is able to represent the effects from solid and CCN aerosols on mean droplet diameter, on the cold precipitation prevailing in the MC3E storm, on the activity of the HM process, and on increased homogeneous freezing aloft. The ACC scheme also represents in-cloud droplet activation and the known SIP mechanisms in convection. This makes it possible to investigate aerosol direct effects and indirect effects on convective clouds on climate.

Acknowledgments. The project was funded through a research grant to Vaughan Phillips (VTJP) from the Swedish Research Council for Sustainable Development ("FORMAS" Award 2018-01795). The award focuses on the effects on clouds and climate arising from the time dependence of ice initiation. Vaughan T.J. Phillips planned and directed the current study. Also, coauthors at Lund were supported by awards to Vaughan T. J. Phillips from the U.S. Department of Energy (DOE) (DE-SC0018932), about ice initiation in clouds, from the Swedish Research Council ("Vetenskapsradet") about bioaerosol effects on clouds, from the U.S. DOE (DESC0018967) with a subaward from Oklahoma University about reasons for high concentrations of ice in clouds, and from Sweden's Innovation Agency (Vinnova) (2020-03406). We would like to extend our sincere gratitude to the contributors of the Community Earth System Model. The authors are grateful to John Truesdale for providing valuable advice and help regarding the CESM.

Data availability statement. The thermodynamic observational dataset for the MC3E is available at https://adc.arm.gov/discovery/#v/results/s/s::varanalmc3e. The observational dataset for cloud microphysical properties is obtained from https://ghrc.nsstc.nasa.gov/pub/fieldCampaigns/gpmValidation/mc3e/. The model output and the post processing scripts are available at https://doi.org/10.5281/zenodo.14606882. The codes for the ACC scheme are available on request from the corresponding author.

APPENDIX A

List of Symbols

Table A1 shows the list of symbols used in this paper.

TABLE A1. List of symbols.

Symbol	Description	Units and/or value
A_X	Fitting constant for the temperature shift in the solid aerosols	—
C_d	Drag coefficient	0.506
D	Molecular diffusion coefficient	$m^2\ s^{-1}$
D_{cw}	Cloud droplet diameter	μm
$D_{droplet}$	Mean diameter of cloud droplet	m
D_g	Geometric mean diameter of aerosol	μm
D_{min}	Minimum threshold for cloud droplet diameter for HM parameterization	μm
D_{max}	Maximum threshold for cloud droplet diameter for HM parameterization	μm
D_x	Equivalent spherical diameter of the cloud microphysical species corresponding to subscript x	m
$D_{X'}$	Geometric mean diameter of aerosol in group X'	m
$D_{x,1}$	Sphere equivalent diameter of the first bin corresponding to subscript x	m
D_u	Detrainment rate	$kg\ m^{-3}\ s^{-1}$
$D^{(1)}_{deep}$	Turbulent detrainment rate	$kg\ m^{-3}\ s^{-1}$
$D^{(2)}_{deep}$	Organized detrainment by loss of buoyancy	$kg\ m^{-3}\ s^{-1}$
$e_i(T)$	Saturation vapor pressure relative to ice at temperature T	Pa
$e_w(T)$	Saturation vapor pressure relative to water at temperature T	Pa
E_{up}	Entrainment rate	$kg\ m^{-3}\ s^{-1}$
E_u	Entrainment rate	s^{-1}
f	Factor for turbulent flow	2
$f_H M$	Droplet size-dependent factor, which is set to 0 for droplets with sizes $< 16\ \mu$m	
g	Gravitational acceleration	$9.8\ m\ s^{-2}$
$H_{X'}$	Fraction reducing IN activity at low	
K	Coefficient of thermal conductivity of air	$J\ m^{-1}\ s^{-1}\ K^{-1}$
K_{up}	Kinetic energy of the updraft	$m^2\ s^{-2}$
L_v	Latent heat of vaporization	$2.5 \times 10^6\ J\ kg^{-1}$
L_s	Latent heat of sublimation	$2.8336 \times 10^6\ J\ kg^{-1}$
m_g	Mass of graupel/hail	kg
$m_y(j)$	Mass mixing ratio of interacting particle y in jth size bin	$kg\ kg^{-1}$
m_s	Mass of snow	kg
M_{up}	Updraft mass flux	$kg\ m^{-2}\ s^{-1}$
$m_{x,1}$	Mass concentration of the hydrometer in first size bin	$kg\ kg^{-1}$
$n(D_x)\ dD_x$	Number concentration of the hydrometer in the size range dD_x	m^{-3}
$N_{aerosol}(I, j)$	Number concentration of ith aerosol in the jth size bin in the solid aerosol group (sulfate in mode 1 and mode 2, secondary organic matter, and sea salt)	kg^{-1}
N_c	Number of cloud droplets	cm^{-3}
NIHMS	Number concentration tendency of cloud-ice splinters generated when liquid accretes onto snow	$kg^{-1}\ s^{-1}$
NIHMG	Number concentration tendency of cloud-ice splinters generated when liquid accretes onto graupel	$kg^{-1}\ s^{-1}$
n_{IN}	Total number concentration of predicted active INPs	kg^{-1}
$n_{IN,1,*}$	Number concentration of reference activity spectrum for water saturation in background-troposphere scenario	kg^{-1}
$n_{IN,X'}$	Contribution to n_{IN} from aerosol group X	kg^{-1}
$n_{IN,X'}$	Number of aerosols in aerosol group X lost by ice nucleation	kg^{-1}
NGAUT	Number concentration tendency for autoconversion of snow to form graupel	$kg^{-1}\ s^{-1}$
NRAUT	Number concentration tendency for autoconversion of cloud liquid to rain	$kg^{-1}\ s^{-1}$
$n_x(i)$	Number concentration of interacting particle x in ith size bin	kg^{-1}
$n_{x,0}$	Intercept of the hydrometeors corresponding to subscript x	—
$n_y(j)$	Number concentration of interacting particle y in jth size bin	kg^{-1}
$n_{x',a}$	Number of aerosols lost by ice nucleation in group X'	kg^{-1}
p_w	Shape parameter for water	3.5
p_i	Shape parameter for cloud ice	1

TABLE A1. (*Continued*)

Symbol	Description	Units and/or value
p_g	Shape parameter for graupel/hail	—
PRAUT	Mass mixing ratio tendency for autoconversion of cloud liquid to rain	kg kg^{-1} s^{-1}
PGACW	Mass mixing ratio tendency for cloud liquid accreting onto graupel	kg kg^{-1} s^{-1}
PGAUT	Mass mixing ratio tendency for autoconversion of snow to form graupel	kg kg^{-1} s^{-1}
PSACW	Mass mixing ratio tendency for cloud liquid accreting onto snow	kg kg^{-1} s^{-1}
PSAUT	Mass mixing ratio tendency for aggregation of cloud ice to form snow	kg kg^{-1} s^{-1}
Q	Passive tracer to calculate the age of the parcel since entering the subzero part of the cloud	kg^{-1}
Q_0	Initial passive tracer value when the parcel is outside the glaciated part of the cloud	1 kg^{-1}
q_v	Vapor mass mixing ratio	kg kg^{-1}
q_c	Cloud droplet mass mixing ratio	kg kg^{-1}
q_i	Cloud-ice mass mixing ratio	kg kg^{-1}
q_s	Snow mass mixing ratio	kg kg^{-1}
q_r	Rain mass mixing ratio	kg kg^{-1}
q_g	Graupel/hail mass mixing ratio	kg kg^{-1}
$r(j)$	Radius of the cloud droplet or cloud ice for the jth bin	m
RH	Fractional relative humidity in the environment	—
R_{det}	Compensation parameter	0.6
r_t	Threshold radius	40 μm
R_v	Gas constant for water vapor	J kg^{-1} K^{-1}
S_{eq}	Equilibrium supersaturation	—
s_i	Fractional supersaturation with respect to ice	—
s_i^w	Value of S_i at water saturation	
s_w	Fractional supersaturation with respect to water	—
s_X	Signifies source/sink term corresponding to subscript X	When X represents mass concentration, then the unit is kg kg^{-1} s^{-1}, and when X represents number concentration, the unit is kg^{-1} s^{-1}
$\tilde{t}$	Age of parcel since entering subzero part of cloud	S
$\Delta\tilde{T}_X$	Temperature shift	K
$T_{v,\text{up}}$	Virtual temperature of the updraft	K
$\overline{T}_v$	Virtual temperature of the environment	K
T	Temperature of the parcel	K
T_{HM}	Triangular function of temperature	
w_{up}	Vertical velocity	m s^{-1}
X	Conserved variables such as mass and number mixing ratio of cloud liquid, cloud ice, rain, snow, graupel/hail, and actual number mixing ratio for each size bin of the aerosols in any given chemical species (e.g., sulfate, dust, and sea salt)	When X represents mass concentration, then the unit is kg kg^{-1}, and when X represents number concentration, the unit is kg^{-1}
X_{env}	Environmental variable corresponding to X	Units of X
$\alpha_{X'}$	Fraction of $n_{\text{IN},1,*}$ from IN activity of group X'	[2/3, 1/3–0.06, 0.06]
β	Constant for vertical velocity calculation	1.875
β_X	Fitting constant for temperature shift in the solid aerosols	—
γ	Virtual mass coefficient	—
δ_{up}	Constant for turbulent detrainment rate calculation	0.75×10^{-4} m^{-1}
Δn_c	Number of cloud droplets generated	kg^{-1}
Δn_i	Number of cloud ice generated	kg^{-1}
$\Delta n_{x,y}$	Change in number concentration for particle x collecting y	kg kg^{-1}
$\Delta q_{x,y}$	Change in mass mixing ratio for particle x collecting y	kg kg^{-1}
Δq_c	Mass mixing ratio of cloud droplets generated	kg kg^{-1}
Δt	Time step for the parcel ascent	0.025 s
δz	Distance by which the parcel ascends	m
Θ_v'	Fractional effective buoyancy which is the fractional difference in virtual effective temperature	—
λ_x	Slope parameter of cloud microphysical properties corresponding to subscript x	—
μ_{up}	Mixing coefficient	kg m^{-3} s^{-1}
$\mu_{X'}$	Average number of ice embryos per aerosol particle in group X'	

TABLE A1. (*Continued*)

Symbol	Description	Units and/or value
$\xi(T)$	Function that is 0 for $T > -2$°C and 1 for $T < -5$°C, being $\xi_1^0(T, -5, -2)$ for $-5 < T < -2$°C	$0 \le \xi \le 1$.
ρ	Air density	kg m^{-3}
ρ_w	Water density	kg m^{-3}
τ_Q	Arbitrary relaxation time	1800 s
χ_{snow}	Snow-rimed fraction	
$\chi_{x,y}$	Collection kernel for the interacting particles x and y	
$\Omega_{X'}$	Total surface area of all aerosols larger than 0.1 μm in group X'	(aerosol) m^2 (air) kg^{-1}
$\Omega_{X',1,*}$	Component of $\Omega_{X'}$ for aerosols in group X' with diameters between 0.1 and 1 μm in background-troposphere scenario	(aerosol) m^2 (air) kg^{-1}

APPENDIX B

Framework for the ZM Scheme

Zhang and McFarlane (1995) [Eqs. (6a)–(6c)] provide the budget for the mean dry static energy, water vapor, and cloud water content:

$$\frac{\partial(M_u S_u)}{\partial z} = (E_u - D_u)S + LC_u, \tag{B1}$$

$$\frac{\partial(M_u q_u)}{\partial z} = E_u - D_u q^* - C_u, \tag{B2}$$

$$\frac{\partial(M_u l)}{\partial z} = -D_u l_d + C_u + R_r. \tag{B3}$$

The temperature in the plume is determined by the following equation:

$$T_u = \frac{S_u - gz}{C_p}, \tag{B4}$$

where T_u is the temperature profile of the bulk plume, S_u is the dry static energy, g is the gravitational acceleration, z is the height above the surface level, and C_p is the specific heat at constant air pressure.

APPENDIX C

Comparison of the Equations for SZ11 and ACC Scheme

a. Cloud-base droplet activation

Ming et al. (2006) work on the linkage between the droplet number concentration, updraft velocity, and chemistry and size distribution of soluble aerosols. This scheme represents how the critical supersaturation for activation is related to the critical dry size of the CCN aerosols.

Solving the Ming et al. (2006) [Eqs. (4), (8), and (10)] gives the value for the condensation rate dW/dt. The aerosol particles are considered activated droplets when their critical supersaturation is lower than the calculated maximum supersaturation:

$$\Delta n_c = \sum_{i=1}^{i=4}\sum_{j=1}^{j=20} N_{\text{aerosol}}(i, j)$$

$$\Delta q_c = \sum_{i=1}^{i=4}\sum_{j=1}^{j=20} \frac{\pi}{6} N_{\text{aerosol}}(i, j) D^3_{p\max}(i, j)\rho_w, \tag{C1}$$

where i is the aerosol particle from the soluble aerosol group (sulfate in mode 1 and mode 2, secondary organic matter, and sea salt) and j is the size bins for each soluble aerosol mode. The terms Δq_c and Δn_c are the mass and number of cloud droplets activated, respectively. The term $N_{\text{aerosol}}(i, j)$ is the activated number of aerosol, and $D_{p\max}$ is the droplet diameter at maximum supersaturation in the jth bin for ith mode.

b. Heterogeneous ice nucleation

The EP is dependent on the loading, chemistry, and surface area of insoluble aerosol species. The EP represents all heterogeneous nucleation processes (contact, immersion, deposition, and condensation followed by freezing) and the scarcity of ice nucleation at subsaturated conditions at temperatures warmer than −35°C. The number concentration of active INPs is represented as

$$n_{\text{IN}} = \sum_X n_{\text{IN},X'}, \tag{C2}$$

where X' represents the aerosol group for species dust (DM), black carbon (BC), insoluble nonbiological organic matter (BIO), and primary biological organic matter (solO). Therefore,

$$n_{\text{IN},X'} = \int_{\log(0.1\mu\text{m})}^{\infty} 1 - \exp(-\mu_{X'}) \times \frac{dn_{X'}}{d\log D_{X'}} d\log D_{X'}, \tag{C3}$$

where $n_{\text{IN},X'}$ is the number concentration of INPs activated by deposition and condensation/immersion-freezing modes from the group X' within the size interval $d\log D_{X'}$. The term $n_{X'}$ is the number concentration of aerosols in group X'. The term $D_{X'}$ is the particle size in group X'. The term $\mu_{X'}$ is the average number of ice embryos per insoluble aerosol particle of size $D_{X'}$:

$$\mu_{X'} = H_{X'}(s_i, T)\xi(T)\frac{\alpha_{X'} n_{IN,1,*}}{\Omega_{X',1,*}} \times \frac{d\Omega_{X'}}{dn_{X'}}$$
$$\text{for } T < 0°\text{C and } 1 < s_i < s_i^w, \tag{C4}$$

where the term $H_{X'}(s_i, T)$ is the empirically determined fraction representing the reduction in the heterogeneous ice nucleation activity in substantially subsaturated conditions. The term $\alpha_{X'}$ is a fractional contribution from aerosol group X'. The term $\Omega_{X'}$ is the total surface area of all insoluble aerosols with dry diameters larger than 0.1 μm, per unit mass of air in group X'. The term $\Omega_{X',1,*}$ is the component of $\Omega_{X'}$ due to aerosols with diameters between 0.1 and 0.01 μm in the background-troposphere scenario. The term $n_{\text{IN},1,*}$ is the number concentration of reference activity spectrum for water saturation in a background activity scenario. The term $\xi(T)$ is a factor set to 0 and unity for temperatures warmer than −2°C and temperatures colder than −5°C. More details are provided in Phillips et al. (2013). The number of cloud ice generated by EP is given by

$$\Delta n_i = \sum_{X'} \max(n_{\text{IN},X'} - n_{X',a}, 0) \equiv \delta n_{X',a}, \tag{C5}$$

where $n_{X',a}$ is the number concentration of INPs from group X' that had already been activated.

c. Hallett–Mossop

The HM process produces a certain number of ice splinters from the riming of snow and graupel/hail for a given mass of supercooled cloud liquid accreted (350 mg^{-1} of rime). Hence,

$$\text{NIHMS} = 350e^6 f_{\text{HM}} T_{\text{HM}} \text{PSACW}$$
$$\text{NIHMG} = 350e^6 f_{\text{HM}} T_{\text{HM}} \text{PGACW}, \tag{C6}$$

where NIHMS and NIHMG are the number concentration tendency of cloud-ice splinters generated from liquid accreted onto snow and graupel, respectively. PSACW and PGACW are the mass mixing ratio tendencies for liquid accretes onto snow and graupel, respectively.

The term f_{HM} is a droplet size-dependent factor given as

$$f_{\text{HM}} = \begin{cases} 0 & \text{if } D_{\text{CW}} < 16\mu\text{m}, \\ 1 & \text{if } D_{\text{CW}} > 24\mu\text{m}, \\ \dfrac{D_{\text{CW}} - D_{\min}}{D_{\max} - D_{\min}} & \text{elsewhere.} \end{cases} \tag{C7}$$

The term T_{HM} is a triangular function of temperature, represented as

$$T_{\text{HM}} = \begin{cases} \dfrac{8 - |T|}{2.5} & \text{if } 5.5° \geq T > -8°\text{C}, \\ 0 & \text{if } T \leq -8° \text{ tor} T > -3°\text{C}, \\ \dfrac{|T| - 3}{2.5} & \text{if } -3° \geq T > -8°\text{C}. \end{cases} \tag{C8}$$

d. Autoconversion of cloud water to rain

The autoconversion of cloud water to rain occurs when

$$\text{PRAUT} = 7.98 \times 10^{10} \times q_c^{4.22} N_c^{-3.01}$$
$$\text{NRAUT} = \text{PRAUT} \Big/ \left(\frac{4\pi\rho_w}{\rho} r_t^3\right), \tag{C9}$$

where PRAUT and NRAUT are the mass mixing ratio tendency and number concentration tendency for the autoconversion of cloud water to rain, respectively. The term q_c is in kilograms per kilogram (kg kg^{-1}) and N_c is in cubic centimeters (cm^3). The term ρ_w is the water density, and $r_t = 40\,\mu$m is the threshold radius.

e. Autoconversion of cloud ice to snow

The autoconversion of cloud ice to snow occurs when

$$\text{PSAUT} = \frac{q_i}{\Delta t}\left[1 - \left(\frac{\lambda_i}{\lambda_{i0}}\right)\right], \tag{C10}$$

where $\lambda_{i0} = \Gamma(2 + \mu_i)/150 \times 10^{-6}\,\Gamma(1 + \mu_i)\}$ for the shape parameter μ_i and Δt is the time step for parcel ascent.

f. Autoconversion of snow to graupel

The conversion of rimed snow to graupel/hail in the bin occurs when the snow-rimed fraction $\chi_{\text{snow}} > 0.5$. The calculation of this snow-rimed fraction follows Gautam (2022).

The number grid n_{snow} and mass grid m_{snow} of 33 size bins are populated using Eqs. (2) and (3), respectively:

$$\text{PGAUT} = \sum_{i=1}^{i=33} \frac{n_{\text{snow}}(i) m_{\text{snow}}(i)}{\Delta t}, \text{ if } \chi_{\text{snow}} > 0.5$$
$$\text{NGAUT} = \sum_{i=1}^{i=33} \frac{n_{\text{snow}}(i)}{\Delta t}, \text{ if } \chi_{\text{snow}} > 0.5, \tag{C11}$$

where PGAUT and NGAUT are the mass and the number concentration tendency of rimed snow to form graupel, respectively. The term i is the index of the size bin, and only bins with $\chi_{\text{snow}} > 0.5$ are considered.

g. Accretion and aggregation processes

For the interacting particle x collecting y, number concentration grid (n_x, n_y) and mass grid (m_x, m_y) of 33 size bins are populated using Eqs. (2) and (3), respectively.

For x collecting y, the change in mass mixing ratio per unit time $\Delta q_{x,y}/\Delta t$ is represented as

$$\frac{\Delta q_{x,y}}{\Delta t} = \sum_{i=1}^{i=33} \sum_{j=1}^{j=33} \chi_{x,y}(i, j) n_x(i) n_y(j) m_y(j). \tag{C12}$$

The change in the number concentration per unit time is e, and $\Delta n_{x,y}/\Delta t$ is represented as

$$\frac{\Delta n_{x,y}}{\Delta t} = \sum_{i=1}^{j=33} \sum_{i=1}^{j=33} \chi_{x,y}(i, j) n_x(i) n_y(j), \tag{C13}$$

where i and j are the indices for summation through all the size bins and $\chi_{x,y}$ is the collection kernel interacting particles x and y.

1) COLLECTION KERNELS

The collection kernel $\chi_{x,y}$ is computed as

$$\chi_{x,y}(i,j) = E_{c,x,y}(i,j)E_{s,x,y}A_{x,y}(i,j)V_t\sqrt{\frac{\rho_{\text{sfc}}}{\rho}}, \tag{C14}$$

where $E_{c,x,y}(i,j)$ is the collision efficiency, and results from Phillips et al. (2005) are used to obtain these values. The term $E_{s,x,y}$ is the sticking efficiency. The term ρ_{sfc} is the surface air density.

The term $A_{x,y}(i,j)$ is the geometric cross-sectional area and is given by

$$A_{x,y}(i,j) = \pi\left[\frac{D_x(j)}{2} - \frac{D_y(j)}{2}\right]^2, \tag{C15}$$

where $D_x(j)$ and $D_y(j)$ are the diameters for the interacting particles x and y, respectively, for jth size bin.

The term V_t is the relative fall velocity, and $V_t = |V_{t,x,\text{sfc}}(i) - V_{t,y,\text{sfc}}(j)|V_{t,x,\text{sfc}}$ and $V_{t,y,\text{sfc}}(j)$ are the terminal velocities for the particles x and y, respectively.

Terminal velocity is given as

$$V_t = AD^B. \tag{C16}$$

The coefficients A and B are given in Heymsfield et al. (2007) [Eq. (5)].

2) STICKING EFFICIENCY

The sticking efficiency for the collision between interacting particles x and y uses an empirical parameterization developed by Phillips et al. (2015) [Eq. (12)]:

$$E_{s,x,y} = \exp\left[\frac{\beta(T)K_c}{\alpha}\right], \tag{C17}$$

where $E_{s,x,y}$ is the sticking efficiency. The term $\beta(T)$ is the temperature-dependent thermal smoothness coefficient that inherent properties of ice such as shape and surface texture. The term K_c is the collision kinetic energy of the colliding particles and is proportional to the energy required to separate these particles after impact. The term α is the surface area of the smaller particle among the colliding particles.

3) TURBULENCE ENHANCEMENT

A turbulent enhancement scheme by Benmoshe and Khain (2014) is implemented. In the ACC scheme, the dissipation rate is empirically parameterized from the data of MacPherson and Isaac (1977). The dissipation rate is ϵ, given by

$$\epsilon = 0.009\,54|w_{\text{up}}|. \tag{C18}$$

APPENDIX D

Figures for Detrainment Rate, Cloud Properties for Sensitivity Simulations and Initial Aerosol Concentration Profile

Figures D1–D4 show the comparison of detrainment rate between the new ACC scheme and the old ZM scheme, comparison of cloud properties between the ACC_{24} and time dependence run, comparison of cloud properties between the ACC_{24} and no coalescence run, and the initial aerosol mass concentration profile.

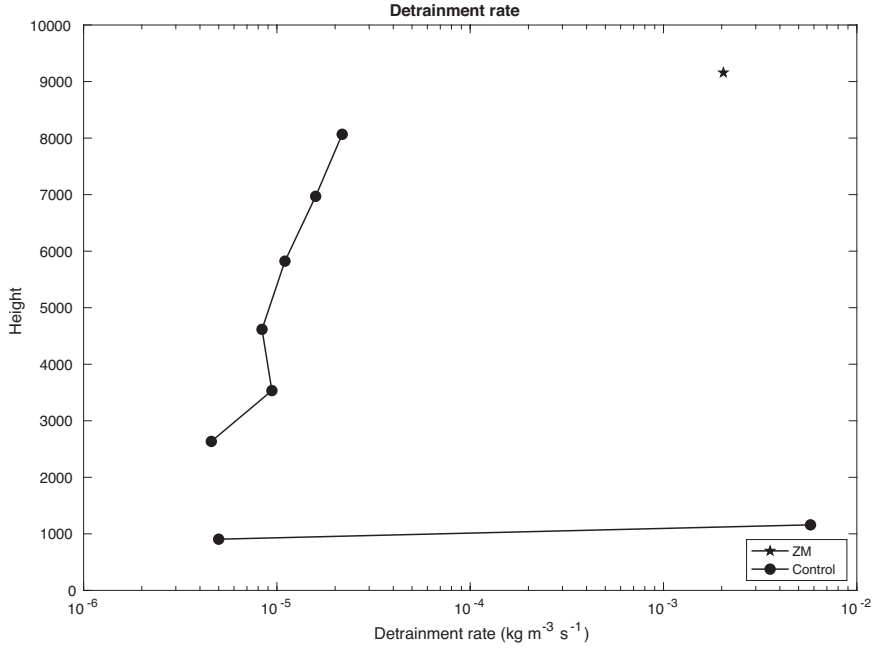

FIG. D1. Comparison of predicted detrainment rate between the ZM parameterization (solid black line with pentagram) (Zhang and McFarlane 1995) and the new scheme (solid black line with circle) described in section 2d(2) at the time of the peak of precipitation rate, i.e., 2300 UTC 11 May 2011.

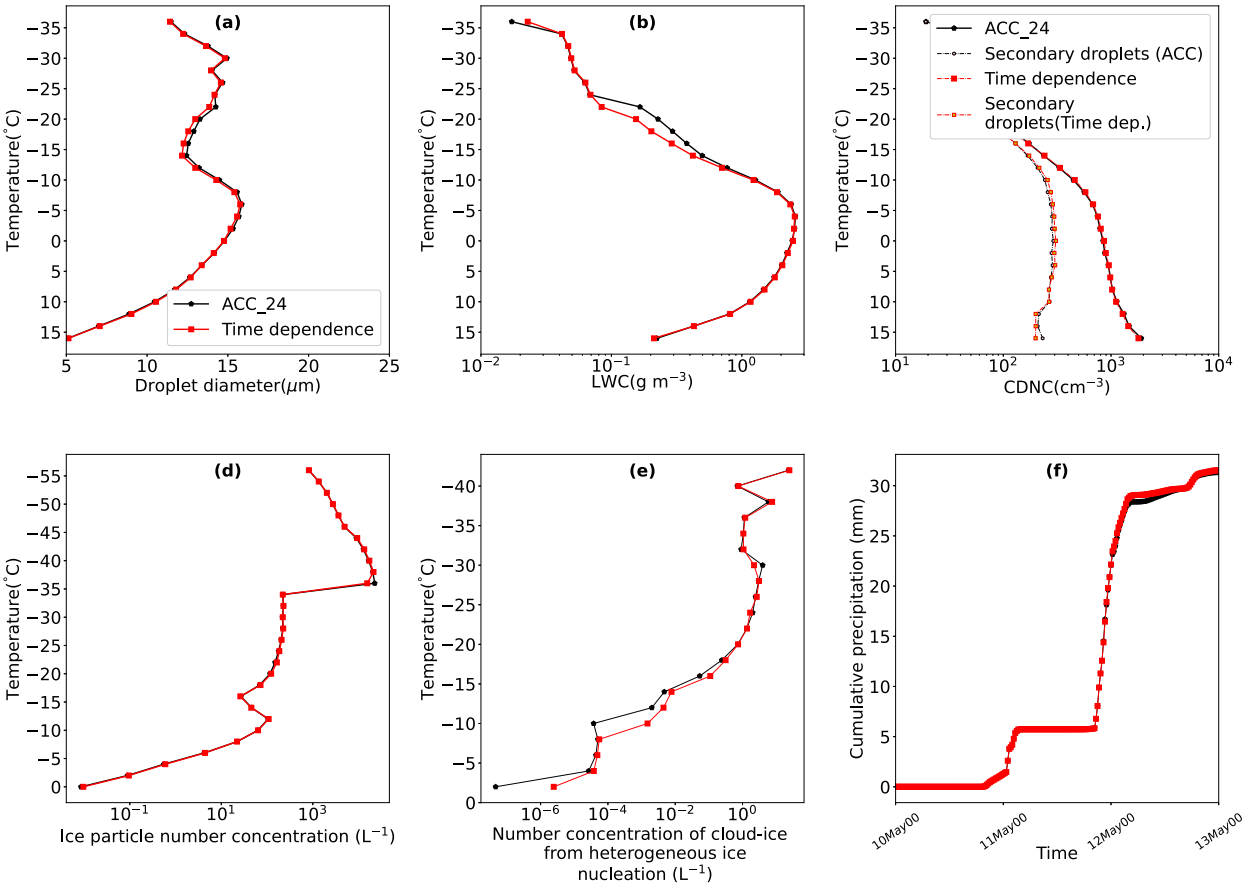

FIG. D2. Predicted (a) mean cloud droplet diameter, (b) LWC, (c) CDNC, (d) total number concentration of ice particles, (e) tagging tracer representing the cloud ice generated by heterogeneous ice nucleation from the time dependence (solid red line with square) and ACC_24 (solid black line with pentagram) simulations. The cloud microphysical properties conditionally averaged over cloudy convective updrafts ($w_{up} > 3$ m s^{-1}). Predicted (f) cumulative surface precipitation from the time dependence (solid red line with square) and ACC_24 (solid black line with pentagram) simulations are plotted.

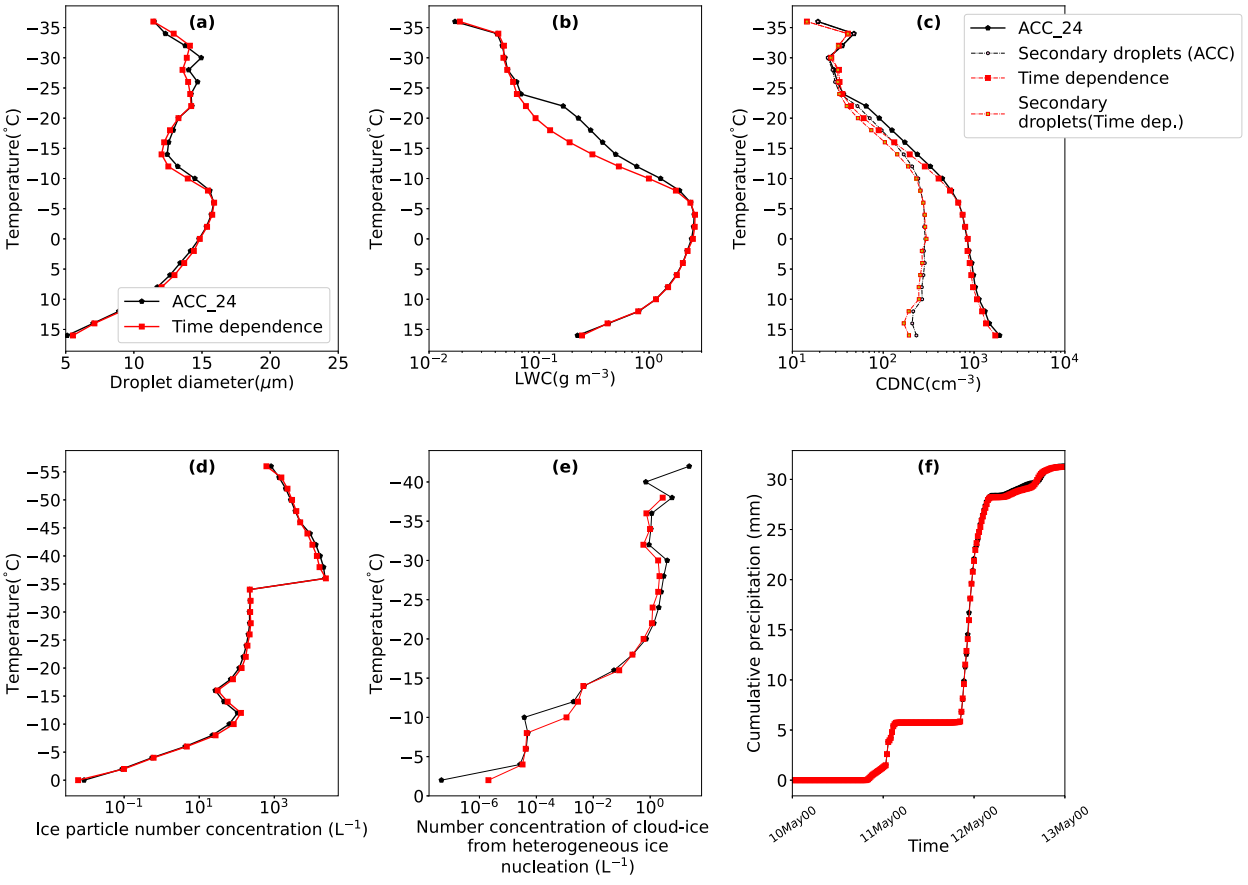

FIG. D3. Predicted (a) mean cloud droplet diameter, (b) predicted LWC, (c) predicted CDNC plotted with secondary droplets, (d) total number concentration of ice particles, (e) precipitation rate, and (f) cumulative surface precipitation from the time dependence (solid red line with square) and ACC_24 (solid black line with pentagram) simulations. The cloud microphysical properties conditionally averaged over cloudy convective updrafts ($w_{up} > 3$ m s^{-1}).

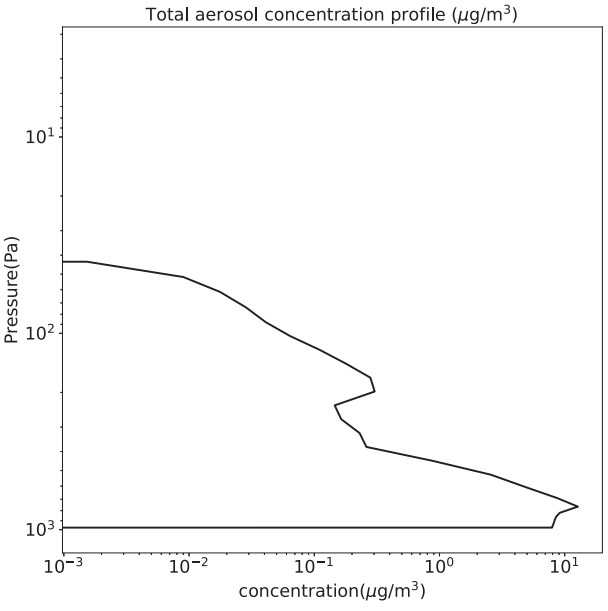

FIG. D4. Vertical profile of initial total aerosol mass concentration (μg m^{-3}).

REFERENCES

Adams-Selin, R. D., and R. H. Johnson, 2013: Examination of gravity waves associated with the 13 March 2003 bow echo. *Mon. Wea. Rev.*, **141**, 3735–3756, https://doi.org/10.1175/MWR-D-12-00343.1.

Albrecht, B. A., 1989: Aerosols, cloud microphysics, and fractional cloudiness. *Science*, **245**, 1227–1230, https://doi.org/10.1126/science.245.4923.1227.

Andreae, M. O., and D. Rosenfeld, 2008: Aerosol–cloud–precipitation interactions. Part 1. The nature and sources of cloud-active aerosols. *Earth-Sci. Rev.*, **89**, 13–41, https://doi.org/10.1016/j.earscirev.2008.03.001.

Andrejczuk, M., W. W. Grabowski, J. Reisner, and A. Gadian, 2010: Cloud-aerosol interactions for boundary layer stratocumulus in the Lagrangian Cloud Model. *J. Geophys. Res.*, **115**, D22214, https://doi.org/10.1029/2010JD014248.

Atlas, R. L., C. S. Bretherton, M. F. Khairoutdinov, and P. N. Blossey, 2022: Hallett-Mossop rime splintering dims cumulus clouds over the Southern Ocean: New insight from nudged global storm-resolving simulations. *AGU Adv.*, **3**, e2021AV000454, https://doi.org/10.1029/2021AV000454.

Bechtold, P., M. Köhler, T. Jung, F. Doblas-Reyes, M. Leutbecher, M. J. Rodwell, F. Vitart, and G. Balsamo, 2008: Advances in simulating atmospheric variability with the ECMWF model: From synoptic to decadal time-scales. *Quart. J. Roy. Meteor. Soc.*, **134**, 1337–1351, https://doi.org/10.1002/qj.289.

Benmoshe, N., and A. P. Khain, 2014: The effects of turbulence on the microphysics of mixed-phase deep convective clouds investigated with a 2-D cloud model with spectral bin microphysics. *J. Geophys. Res. Atmos.*, **119**, 207–221, https://doi.org/10.1002/2013JD020118.

Boucher, O., and Coauthors, 2013: Clouds and aerosols. *Climate Change 2013: The Physical Science Basis*, T. F. Stocker et al., Eds., Cambridge University Press, 571–657.

Bryan, G. H., and H. Morrison, 2012: Sensitivity of a simulated squall line to horizontal resolution and parameterization of microphysics. *Mon. Wea. Rev.*, **140**, 202–225, https://doi.org/10.1175/MWR-D-11-00046.1.

Cantrell, W., and A. Heymsfield, 2005: Production of ice in tropospheric clouds: A review. *Bull. Amer. Meteor. Soc.*, **86**, 795–808, https://doi.org/10.1175/BAMS-86-6-795.

Chandrakar, K. K., W. W. Grabowski, H. Morrison, and G. H. Bryan, 2021: Impact of entrainment mixing and turbulent fluctuations on droplet size distributions in a cumulus cloud: An investigation using Lagrangian microphysics with a subgrid-scale model. *J. Atmos. Sci.*, **78**, 2983–3005, https://doi.org/10.1175/JAS-D-20-0281.1.

Cheng, L., T.-C. Yip, and H.-R. Cho, 1980: Determination of mean cumulus cloud vorticity from GATE A/B-scale potential vorticity budget. *J. Atmos. Sci.*, **37**, 797–811, https://doi.org/10.1175/1520-0469(1980)037<0797:DOMCCV>2.0.CO;2.

Chin, M., R. B. Rood, S.-J. Lin, J.-F. Müller, and A. M. Thompson, 2000: Atmospheric sulfur cycle simulated in the global model GOCART: Model description and global properties. *J. Geophys. Res.*, **105**, 24 671–24 687, https://doi.org/10.1029/2000JD900384.

Christensen, M. W., P.-L. Ma, P. Wu, A. C. Varble, J. Mülmenstädt, and J. D. Fast, 2023: Evaluation of aerosol–cloud interactions in E3SM using a Lagrangian framework. *Atmos. Chem. Phys.*, **23**, 2789–2812, https://doi.org/10.5194/acp-23-2789-2023.

Connolly, P. J., T. W. Choularton, M. W. Gallagher, K. N. Bower, M. J. Flynn, and J. A. Whiteway, 2006: Cloud-resolving simulations of intense tropical *Hector* thunderstorms: Implications for aerosol–cloud interactions. *Quart. J. Roy. Meteor. Soc.*, **132**, 3079–3106, https://doi.org/10.1256/qj.05.86.

Crosier, J., and Coauthors, 2011: Observations of ice multiplication in a weakly convective cell embedded in supercooled mid-level stratus. *Atmos. Chem. Phys.*, **11**, 257–273, https://doi.org/10.5194/acp-11-257-2011.

Danabasoglu, G., and Coauthors, 2020: The Community Earth System Model version 2 (CESM2). *J. Adv. Model. Earth Syst.*, **12**, e2019MS001916, https://doi.org/10.1029/2019MS001916.

DeMott, P. J., D. J. Cziczo, A. J. Prenni, D. M. Murphy, S. M. Kreidenweis, D. S. Thomson, R. Borys, and D. C. Rogers, 2003: Measurements of the concentration and composition of nuclei for cirrus formation. *Proc. Natl. Acad. Sci. USA*, **100**, 14 655–14 660, https://doi.org/10.1073/pnas.2532677100.

——, and Coauthors, 2016: Sea spray aerosol as a unique source of ice nucleating particles. *Proc. Natl. Acad. Sci. USA*, **113**, 5797–5803, https://doi.org/10.1073/pnas.1514034112.

Derbyshire, S. H., A. V. Maidens, S. F. Milton, R. A. Stratton, and M. R. Willett, 2011: Adaptive detrainment in a convective parametrization. *Quart. J. Roy. Meteor. Soc.*, **137**, 1856–1871, https://doi.org/10.1002/qj.875.

de Rooy, W. C., and Coauthors, 2013: Entrainment and detrainment in cumulus convection: An overview. *Quart. J. Roy. Meteor. Soc.*, **139** (670), 1–19, https://doi.org/10.1002/qj.1959.

Donner, L. J., and V. T. Phillips, 2003: Boundary layer control on convective available potential energy: Implications for cumulus parameterization. *J. Geophys. Res.*, **108**, 4701, https://doi.org/10.1029/2003JD003773.

——, C. J. Seman, R. S. Hemler, and S. Fan, 2001: A cumulus parameterization including mass fluxes, convective vertical velocities, and mesoscale effects: Thermodynamic and hydrological aspects in a general circulation model. *J. Climate*, **14**, 3444–3463, https://doi.org/10.1175/1520-0442(2001)014<3444:ACPIMF>2.0.CO;2.

ECMWF, 2021: IFS documentation CY47R3 - Part IV physical processes. ECMWF IFS Doc. 4, ECMWF, 232 pp., https://doi.org/10.21957/eyrpir4vj.

Emanuel, K. A., 1993: A cumulus representation based on the episodic mixing model: The importance of mixing and microphysics in predicting humidity. *The Representation of Cumulus Convection in Numerical Models*, *Meteor. Monogr.*, No. 45, Amer. Meteor. Soc., 185–192, https://doi.org/10.1007/978-1-935704-13-3_19.

Ferrier, B. S., 1994: A double-moment multiple-phase four-class bulk ice scheme. Part I: Description. *J. Atmos. Sci.*, **51**, 249–280, https://doi.org/10.1175/1520-0469(1994)051%3C0249:ADMMPF%3E2.0.CO;2.

Field, P. R., and A. J. Heymsfield, 2015: Importance of snow to global precipitation. *Geophys. Res. Lett.*, **42**, 9512–9520, https://doi.org/10.1002/2015GL065497.

——, ——, and A. Bansemer, 2006: Shattering and particle interarrival times measured by optical array probes in ice clouds. *J. Atmos. Oceanic Technol.*, **23**, 1357–1371, https://doi.org/10.1175/JTECH1922.1.

——, and Coauthors, 2017: Secondary ice production: Current state of the science and recommendations for the future. *Ice Formation and Evolution in Clouds and Precipitation: Measurement and Modeling Challenges*, *Meteor. Monogr.*, No. 58, Amer. Meteor. Soc., https://doi.org/10.1175/AMSMONOGRAPHS-D-16-0014.1.

Forster, P., and Coauthors, 2021: The Earth's energy budget, climate feedbacks, and climate sensitivity. *Climate Change 2021: The Physical Science Basis*, V. Masson-Delmotte et al., Eds., Cambridge University Press, 923–1054.

Fridlind, A. M., and Coauthors, 2004: Evidence for the predominance of mid-tropospheric aerosols as subtropical anvil cloud nuclei. *Science*, **304**, 718–722, https://doi.org/10.1126/science.1094947.

——, A. S. Ackerman, G. McFarquhar, G. Zhang, M. R. Poellot, P. J. DeMott, A. J. Prenni, and A. J. Heymsfield, 2007: Ice properties of single-layer stratocumulus during the Mixed-Phase Arctic Cloud Experiment: 2. Model results. *J. Geophys. Res.*, **112**, D24202, https://doi.org/10.1029/2007JD008646.

Gautam, M., 2022: Fragmentation in graupel snow collisions. M.S. thesis, Dept. of Physical Geography and Ecosystem Science, Lund University, 47 pp., http://lup.lub.lu.se/student-papers/record/9087233.

Gettelman, A., and Coauthors, 2010: Global simulations of ice nucleation and ice supersaturation with an improved cloud scheme in the Community Atmosphere Model. *J. Geophys. Res.*, **115**, D18216, https://doi.org/10.1029/2009JD013797.

——, H. Morrison, K. Thayer-Calder, and C. M. Zarzycki, 2019a: The impact of rimed ice hydrometeors on global and regional climate. *J. Adv. Model. Earth Syst.*, **11**, 1543–1562, https://doi.org/10.1029/2018MS001488.

——, J. E. Truesdale, J. T. Bacmeister, P. M. Caldwell, R. B. Neale, P. A. Bogenschutz, and I. R. Simpson, 2019b: The Single Column Atmosphere Model version 6 (SCAM6): Not a scam but a tool for model evaluation and development. *J. Adv. Model. Earth Syst.*, **11**, 1381–1401, https://doi.org/10.1029/2018MS001578.

Grandpeix, J.-Y., V. Phillips, and R. Tailleux, 2004: Improved mixing representation in Emanuel's convection scheme. *Quart. J. Roy. Meteor. Soc.*, **130**, 3207–3222, https://doi.org/10.1256/qj.03.144.

Gupta, A. K., and Coauthors, 2023: The microphysics of the warm-rain and ice crystal processes of precipitation in simulated continental convective storms. *Commun. Earth Environ.*, **4**, 226, https://doi.org/10.1038/s43247-023-00884-5.

Hallett, J., and S. C. Mossop, 1974: Production of secondary ice particles during the riming process. *Nature*, **249**, 26–28, https://doi.org/10.1038/249026a0.

Harris-Hobbs, R. L., and W. A. Cooper, 1987: Field evidence supporting quantitative predictions of secondary ice production rates. *J. Atmos. Sci.*, **44**, 1071–1082, https://doi.org/10.1175/1520-0469(1987)044<1071:FESQPO>2.0.CO;2.

Hartmann, S., J. Seidel, A. Keinert, A. Kiselev, T. Leisner, and F. Stratmann, 2023: Secondary ice production—No evidence of a productive rime-splintering mechanisms during dry and wet growth. *EGU General Assembly 2023*, Vienna, Austria, European Geosciences Union, Abstract EGU23-11199, https://doi.org/10.5194/egusphere-egu23-11199.

Heymsfield, A. J., L. M. Miloshevich, C. Schmitt, A. Bansemer, C. Twohy, M. R. Poellot, A. Fridlind, and H. Gerber, 2005: Homogeneous ice nucleation in subtropical and tropical convection and its influence on cirrus anvil microphysics. *J. Atmos. Sci.*, **62**, 41–64, https://doi.org/10.1175/JAS-3360.1.

——, A. Bansemer, and C. H. Twohy, 2007: Refinements to ice particle mass dimensional and terminal velocity relationships for ice clouds. Part I: Temperature dependence. *J. Atmos. Sci.*, **64**, 1047–1067, https://doi.org/10.1175/JAS3890.1.

Houze, R. A., Jr., 2014: *Cloud Dynamics*. 2nd ed. Vol. 104, Elsevier, 496 pp.

Huang, J.-D., and C.-M. Wu, 2022: A framework to evaluate convective aggregation: Examples with different microphysics schemes. *J. Geophys. Res. Atmos.*, **127**, e2021JD035886, https://doi.org/10.1029/2021JD035886.

Huang, Y., A. M. Blyth, P. R. A. Brown, T. W. Choularton, and Z. Cui, 2017: Factors controlling secondary ice production in cumulus clouds. *Quart. J. Roy. Meteor. Soc.*, **143**, 1021–1031, https://doi.org/10.1002/qj.2987.

Jakobsson, J. K. F., D. B. Waman, V. T. J. Phillips, and T. B. Kristensen, 2022: Time dependence of heterogeneous ice nucleation by ambient aerosols: Laboratory observations and a formulation for models. *Atmos. Chem. Phys.*, **22**, 6717–6748, https://doi.org/10.5194/acp-22-6717-2022.

James, R. L., V. T. J. Phillips, and P. J. Connolly, 2021: Secondary ice production during the break-up of freezing water drops on impact with ice particles. *Atmos. Chem. Phys.*, **21**, 18 519–18 530, https://doi.org/10.5194/acp-21-18519-2021.

Jefferson, A., 2011: Aerosol Observing System (AOS) handbook. ARM Tech. Rep. DOE/SC-ARM/TR-014, 32 pp., https://doi.org/10.2172/1020729.

Jensen, M. P., and Coauthors, 2016: The Midlatitude Continental Convective Clouds Experiment (MC3E). *Bull. Amer. Meteor. Soc.*, **97**, 1667–1686, https://doi.org/10.1175/BAMS-D-14-00228.1.

Kanji, Z. A., L. A. Ladino, H. Wex, Y. Boose, M. Burkert-Kohn, D. J. Cziczo, and M. Krämer, 2017: Overview of ice nucleating particles. *Ice Formation and Evolution in Clouds and Precipitation: Measurement and Modeling Challenges*, *Meteor. Monogr.*, No. 58, Amer. Meteor. Soc., https://doi.org/10.1175/AMSMONOGRAPHS-D-16-0006.1.

Khain, A., A. Pokrovsky, M. Pinsky, A. Seifert, and V. Phillips, 2004: Simulation of effects of atmospheric aerosols on deep turbulent convective clouds using a spectral microphysics mixed-phase cumulus cloud model. Part I: Model description and possible applications. *J. Atmos. Sci.*, **61**, 2963–2982, https://doi.org/10.1175/JAS-3350.1.

Kogan, Y., 2013: A cumulus cloud microphysics parameterization for cloud-resolving models. *J. Atmos. Sci.*, **70**, 1423–1436, https://doi.org/10.1175/JAS-D-12-0183.1.

Korolev, A., and T. Leisner, 2020: Review of experimental studies of secondary ice production. *Atmos. Chem. Phys.*, **20**, 11 767–11 797, https://doi.org/10.5194/acp-20-11767-2020.

Korolev, A. V., E. F. Emery, J. W. Strapp, S. G. Cober, G. A. Isaac, M. Wasey, and D. Marcotte, 2011: Small ice particles in tropospheric clouds: Fact or artifact? airborne icing instrumentation evaluation experiment. *Bull. Amer. Meteor. Soc.*, **92**, 967–973, https://doi.org/10.1175/2010BAMS3141.1.

Kudzotsa, I., and Coauthors, 2016: Aerosol indirect effects on glaciated clouds. Part I: Model description. *Quart. J. Roy. Meteor. Soc.*, **142**, 1958–1969, https://doi.org/10.1002/qj.2791.

Ladino, L. A., A. Korolev, I. Heckman, M. Wolde, A. M. Fridlind, and A. S. Ackerman, 2017: On the role of ice-nucleating aerosol in the formation of ice particles in tropical mesoscale convective systems. *Geophys. Res. Lett.*, **44**, 1574–1582, https://doi.org/10.1002/2016GL072455.

Lasher-Trapp, S., D. C. Leon, P. J. DeMott, C. M. Villanueva-Birriel, A. V. Johnson, D. H. Moser, C. S. Tully, and W. Wu, 2016: A multisensor investigation of rime splintering in Tropical Maritime Cumuli. *J. Atmos. Sci.*, **73**, 2547–2564, https://doi.org/10.1175/JAS-D-15-0285.1.

Lin, Y.-L., R. D. Farley, and H. D. Orville, 1983: Bulk parameterization of the snow field in a cloud model. *J. Climate*

Appl. Meteor., **22**, 1065–1092, https://doi.org/10.1175/1520-0450(1983)022<1065:BPOTSF>2.0.CO;2.

Liu, X., and J. E. Penner, 2005: Ice nucleation parameterization for global models. *Meteor. Z.*, **14**, 499–514, https://doi.org/10.1127/0941-2948/2005/0059.

——, P.-L. Ma, H. Wang, S. Tilmes, B. Singh, R. C. Easter, S. J. Ghan, and P. J. Rasch, 2016: Description and evaluation of a new four-mode version of the Modal Aerosol Module (MAM4) within version 5.3 of the Community Atmosphere Model. *Geosci. Model Dev.*, **9**, 505–522, https://doi.org/10.5194/gmd-9-505-2016.

Lohmann, U., 2006: Aerosol effects on clouds and climate. *Space Sci. Rev.*, **125**, 129–137.

Mace, G. G., Q. Zhang, M. Vaughan, R. Marchand, G. Stephens, C. Trepte, and D. Winker, 2009: A description of hydrometeor layer occurrence statistics derived from the first year of merged Cloudsat and CALIPSO data. *J. Geophys. Res.*, **114**, D00A26, https://doi.org/10.1029/2007JD009755.

MacPherson, J. I., and G. A. Isaac, 1977: Turbulent characteristics of some Canadian cumulus clouds. *J. Appl. Meteor.*, **16**, 81–90, https://doi.org/10.1175/1520-0450(1977)016%3C0081:TCOSCC%3E2.0.CO;2.

Marcolli, C., S. Gedamke, T. Peter, and B. Zobrist, 2007: Efficiency of immersion mode ice nucleation on surrogates of mineral dust. *Atmos. Chem. Phys.*, **7**, 5081–5091, https://doi.org/10.5194/acp-7-5081-2007.

Ming, Y., V. Ramaswamy, L. J. Donner, and V. T. J. Phillips, 2006: A new parameterization of cloud droplet activation applicable to General Circulation Models. *J. Atmos. Sci.*, **63**, 1348–1356, https://doi.org/10.1175/JAS3686.1.

Morrison, H., and A. Gettelman, 2008: A new two-moment bulk stratiform cloud microphysics scheme in the Community Atmosphere Model, version 3 (CAM3). Part I: Description and numerical tests. *J. Climate*, **21**, 3642–3659, https://doi.org/10.1175/2008JCLI2105.1.

Mülmenstädt, J., O. Sourdeval, J. Delanoë, and J. Quaas, 2015: Frequency of occurrence of rain from liquid-, mixed-, and ice-phase clouds derived from A-Train satellite retrievals. *Geophys. Res. Lett.*, **42**, 6502–6509, https://doi.org/10.1002/2015GL064604.

Ochs, H. T., III, 1978: Moment-conserving techniques for warm cloud microphysical computation. Part II. Model testing and results. *J. Atmos. Sci.*, **35**, 1959–1973, https://doi.org/10.1175/1520-0469(1978)035<1959:MCTFWC>2.0.CO;2.

O'Shea, S., and Coauthors, 2021: Characterising optical array particle imaging probes: Implications for small-ice-crystal observations. *Atmos. Meas. Tech.*, **14**, 1917–1939, https://doi.org/10.5194/amt-14-1917-2021.

Patade, S., and Coauthors, 2022: The influence of multiple groups of biological ice nucleating particles on microphysical properties of mixed-phase clouds observed during MC3E. *Atmos. Chem. Phys.*, **22**, 12 055–12 075, https://doi.org/10.5194/acp-22-12055-2022.

Petters, M. D., and S. M. Kreidenweis, 2007: A single parameter representation of hygroscopic growth and cloud condensation nucleus activity. *Atmos. Chem. Phys.*, **7**, 1961–1971, https://doi.org/10.5194/acp-7-1961-2007.

Phillips, V. T. J., 2022: Theory of in-cloud activation of aerosols and microphysical quasi-equilibrium in a deep updraft. *J. Atmos. Sci.*, **79**, 1865–1886, https://doi.org/10.1175/JAS-D-21-0176.1.

——, 2024: A theory for the balance between warm rain and ice crystal processes of precipitation in mixed-phase clouds. *J. Atmos. Sci.*, **81**, 317–339, https://doi.org/10.1175/JAS-D-23-0054.1.

——, and Coauthors, 2005: Anvil glaciation in a deep cumulus updraught over Florida simulated with the explicit microphysics model. I: Impact of various nucleation processes. *Quart. J. Roy. Meteor. Soc.*, **131**, 2019–2046, https://doi.org/10.1256/qj.04.85.

——, L. J. Donner, and S. T. Garner, 2007: Nucleation processes in deep convection simulated by a cloud-system-resolving model with double-moment bulk microphysics. *J. Atmos. Sci.*, **64**, 738–761, https://doi.org/10.1175/JAS3869.1.

——, P. J. DeMott, and C. Andronache, 2008: An empirical parameterization of heterogeneous ice nucleation for multiple chemical species of aerosol. *J. Atmos. Sci.*, **65**, 2757–2783, https://doi.org/10.1175/2007JAS2546.1.

——, and Coauthors, 2009: Potential impacts from biological aerosols on ensembles of continental clouds simulated numerically. *Biogeosciences*, **6**, 987–1014, https://doi.org/10.5194/bg-6-987-2009.

——, P. J. Demott, C. Andronache, K. A. Pratt, K. A. Prather, R. Subramanian, and C. Twohy, 2013: Improvements to an empirical parameterization of heterogeneous ice nucleation and its comparison with observations. *J. Atmos. Sci.*, **70**, 378–409, https://doi.org/10.1175/JAS-D-12-080.1.

——, M. Formenton, A. Bansemer, I. Kudzotsa, and B. Lienert, 2015: A parameterization of sticking efficiency for collisions of snow and graupel with ice crystals: Theory and comparison with observations. *J. Atmos. Sci.*, **72**, 4885–4902, https://doi.org/10.1175/JAS-D-14-0096.1.

——, J.-I. Yano, and A. Khain, 2017a: Ice multiplication by breakup in ice–ice collisions. Part I: Theoretical formulation. *J. Atmos. Sci.*, **74**, 1705–1719, https://doi.org/10.1175/JAS-D-16-0224.1.

——, and Coauthors, 2017b: Ice multiplication by breakup in ice–ice collisions. Part II: Numerical simulations. *J. Atmos. Sci.*, **74**, 2789–2811, https://doi.org/10.1175/JAS-D-16-0223.1.

——, S. Patade, J. Gutierrez, and A. Bansemer, 2018: Secondary ice production by fragmentation of freezing drops: Formulation and theory. *J. Atmos. Sci.*, **75**, 3031–3070, https://doi.org/10.1175/JAS-D-17-0190.1.

——, and Coauthors, 2020: Multiple environmental influences on the lightning of cold-based continental cumulonimbus clouds. Part I: Description and validation of model. *J. Atmos. Sci.*, **77**, 3999–4024, https://doi.org/10.1175/JAS-D-19-0200.1.

Pinsky, M. B., and A. P. Khain, 2002: Effects of in-cloud nucleation and turbulence on droplet spectrum formation in cumulus clouds. *Quart. J. Roy. Meteor. Soc.*, **128**, 501–533, https://doi.org/10.1256/003590002321042072.

Poellot, M. R., and J. C. Pflaum, 1989: Microphysical characteristics of some convective clouds over Oklahoma. *Atmos. Res.*, **24**, 123–136, https://doi.org/10.1016/0169-8095(89)90041-0.

Prabha, T. V., A. Khain, R. S. Maheshkumar, G. Pandithurai, J. R. Kulkarni, M. Konwar, and B. N. Goswami, 2011: Microphysics of premonsoon and monsoon clouds as seen from in situ measurements during the Cloud Aerosol Interaction and Precipitation Enhancement Experiment (CAIPEEX). *J. Atmos. Sci.*, **68**, 1882–1901, https://doi.org/10.1175/2011JAS3707.1.

Pruppacher, H., and J. Klett, 2010: *Microphysics of Clouds and Precipitation*. Atmospheric and Oceanographic Sciences Library, Vol. 18, Springer, 954 pp., https://doi.org/10.1007/978-0-306-48100-0.

Ramanathan, V., R. D. Cess, E. F. Harrison, P. Minnis, B. R. Barkstrom, E. Ahmad, and D. Hartmann, 1989: Cloud-

radiative forcing and climate: Results from the Earth Radiation Budget Experiment. *Science*, **243**, 57–63, https://doi.org/10.1126/science.243.4887.57.

Raval, A., and V. Ramanathan, 1989: Observational determination of the greenhouse effect. *Nature*, **342**, 758–761, https://doi.org/10.1038/342758a0.

Richardson, M. S., and Coauthors, 2007: Measurements of heterogeneous ice nuclei in the western United States in springtime and their relation to aerosol characteristics. *J. Geophys. Res.*, **112**, D02209, https://doi.org/10.1029/2006JD007500.

Rogers, R. R., and M. K. Yau, 1989: *A Short Course in Cloud Physics*. 3rd ed. Elsevier, 290 pp.

Rosenfeld, D., and W. L. Woodley, 2000: Deep convective clouds with sustained supercooled liquid water down to −37.5°C. *Nature*, **405**, 440–442, https://doi.org/10.1038/35013030.

Simpson, J., and V. Wiggert, 1969: Models of precipitating cumulus towers. *Mon. Wea. Rev.*, **97**, 471–489, https://doi.org/10.1175/1520-0493(1969)097<0471:MOPCT>2.3.CO;2.

Song, X., and G. J. Zhang, 2011: Microphysics parameterization for convective clouds in a global climate model: Description and single-column model tests. *J. Geophys. Res.*, **116**, D02201, https://doi.org/10.1029/2010JD014833.

Sotiropoulou, G., S. Sullivan, J. Savre, G. Lloyd, T. Lachlan-Cope, A. M. L. Ekman, and A. Nenes, 2020: The impact of secondary ice production on Arctic stratocumulus. *Atmos. Chem. Phys.*, **20**, 1301–1316, https://doi.org/10.5194/acp-20-1301-2020.

——, E. Vignon, G. Young, H. Morrison, S. J. O'Shea, T. Lachlan-Cope, A. Berne, and A. Nenes, 2021: Secondary ice production in summer clouds over the Antarctic coast: An underappreciated process in atmospheric models. *Atmos. Chem. Phys.*, **21**, 755–771, https://doi.org/10.5194/acp-21-755-2021.

Storelvmo, T., J. E. Kristjánsson, and U. Lohmann, 2008: Aerosol influence on mixed-phase clouds in CAM-Oslo. *J. Atmos. Sci.*, **65**, 3214–3230, https://doi.org/10.1175/2008JAS2430.1.

Stubenrauch, C. J., and Coauthors, 2013: Assessment of global cloud datasets from satellites: Project and database initiated by the GEWEX Radiation Panel. *Bull. Amer. Meteor. Soc.*, **94**, 1031–1049, https://doi.org/10.1175/BAMS-D-12-00117.1.

Sullivan, S. C., C. Hoose, and A. Nenes, 2017: Investigating the contribution of secondary ice production to in-cloud ice crystal numbers. *J. Geophys. Res. Atmos.*, **122**, 9391–9412, https://doi.org/10.1002/2017JD026546.

——, ——, A. Kiselev, T. Leisner, and A. Nenes, 2018: Initiation of secondary ice production in clouds. *Atmos. Chem. Phys.*, **18**, 1593–1610, https://doi.org/10.5194/acp-18-1593-2018.

Sun, Z., and K. P. Shine, 1994: Studies of the radiative properties of ice and mixed-phase clouds. *Quart. J. Roy. Meteor. Soc.*, **120**, 111–137, https://doi.org/10.1002/qj.49712051508.

Takahashi, H., and Z. Luo, 2012: Where is the level of neutral buoyancy for deep convection? *Geophys. Res. Lett.*, **39**, L15809, https://doi.org/10.1029/2012GL052638.

——, Z. J. Luo, and G. L. Stephens, 2017: Level of neutral buoyancy, deep convective outflow, and convective core: New perspectives based on 5 years of CloudSat data. *J. Geophys. Res. Atmos.*, **122**, 2958–2969, https://doi.org/10.1002/2016JD025969.

Takahashi, T., Y. Nagao, and Y. Kushiyama, 1995: Possible high ice particle production during Graupel–Graupel collisions. *J. Atmos. Sci.*, **52**, 4523–4527, https://doi.org/10.1175/1520-0469(1995)052<4523:PHIPPD>2.0.CO;2.

Twohy, C. H., and Coauthors, 2009: Saharan dust particles nucleate droplets in eastern Atlantic clouds. *Geophys. Res. Lett.*, **36**, L01807, https://doi.org/10.1029/2008GL035846.

Twomey, S., 1974: Pollution and the planetary albedo. *Atmos. Environ.*, **8**, 1251–1256, https://doi.org/10.1016/0004-6981(74)90004-3.

——, 1977: The influence of pollution on the shortwave albedo of clouds. *J. Atmos. Sci.*, **34**, 1149–1152, https://doi.org/10.1175/1520-0469(1977)034<1149:TIOPOT>2.0.CO;2.

Uin, J., and O. Enekwizu, 2024: Cloud Condensation Nuclei Particle Counter (CCN) instrument handbook. ARM Tech. Rep. DOE/SC-ARM-TR-168, 15 pp., https://doi.org/10.2172/1251411.

Vardiman, L., 1978: The generation of secondary ice particles in clouds by crystal–crystal collision. *J. Atmos. Sci.*, **35**, 2168–2180, https://doi.org/10.1175/1520-0469(1978)035%3C2168:TGOSIP%3E2.0.CO;2.

Waman, D., S. Patade, A. Jadav, A. Deshmukh, A. K. Gupta, V. T. J. Phillips, A. Bansemer, and P. J. DeMott, 2022: Dependencies of four mechanisms of secondary ice production on cloud-top temperature in a continental convective storm. *J. Atmos. Sci.*, **79**, 3375–3404, https://doi.org/10.1175/JAS-D-21-0278.1.

——, A. Deshmukh, A. Jadav, S. Patade, M. Gautam, V. Phillips, A. Bansemer, and J. Jakobsson, 2023: Effects from time dependence of ice nucleus activity for contrasting cloud types. *J. Atmos. Sci.*, **80**, 2013–2039, https://doi.org/10.1175/JAS-D-22-0187.1.

Wu, D., X. Dong, B. Xi, Z. Feng, A. Kennedy, G. Mullendore, M. Gilmore, and W.-K. Tao, 2013: Impacts of microphysical scheme on convective and stratiform characteristics in two high precipitation squall line events. *J. Geophys. Res. Atmos.*, **118**, 11 119–11 135, https://doi.org/10.1002/jgrd.50798.

Xie, S., Y. Zhang, S. E. Giangrande, M. P. Jensen, R. McCoy, and M. Zhang, 2014: Interactions between cumulus convection and its environment as revealed by the MC3E sounding array. *J. Geophys. Res. Atmos.*, **119**, 11 784–11 808, https://doi.org/10.1002/2014JD022011.

Yang, J., Z. Wang, A. J. Heymsfield, and J. R. French, 2016: Characteristics of vertical air motion in isolated convective clouds. *Atmos. Chem. Phys.*, **16**, 10 159–10 173, https://doi.org/10.5194/acp-16-10159-2016.

Yano, J.-I., and V. T. J. Phillips, 2011: Ice–ice collisions: An ice multiplication process in atmospheric clouds. *J. Atmos. Sci.*, **68**, 322–333, https://doi.org/10.1175/2010JAS3607.1.

Zhang, G. J., and N. A. McFarlane, 1995: Sensitivity of climate simulations to the parameterization of cumulus convection in the Canadian climate centre general circulation model. *Atmos.–Ocean*, **33**, 407–446, https://doi.org/10.1080/07055900.1995.9649539.